The Astrophysical Journal, 716:792–809, 2010 June 10 doi:10.1088/0004-637X/716/1/792


# DEEP $K_s$-NEAR-INFRARED SURFACE PHOTOMETRY OF 80 DWARF IRREGULAR GALAXIES IN THE LOCAL VOLUME

Robin L. Fingerhut[1], Marshall L. McCall[1], Mauricio Argote[1], Michelle E. Cluver[2], Shogo Nishiyama[3], Rami T. F. Rekola[4], Michael G. Richer[5], Ovidiu Vaduvescu[6,7,8], and Patrick A. Woudt[9]
[1] Department of Physics and Astronomy, York University, 4700 Keele Street, Toronto, Ontario M3J 1P3, Canada; rfinger@yorku.ca, mccall@yorku.ca, argote@yorku.ca
[2] IPAC, California Institute of Technology, MC 220-6, Pasadena, CA 91106, USA; mcluver@ipac.caltech.edu
[3] Department of Astronomy, Kyoto University Kitashirakawa-Oiwake-cho, Sakyo-ku, Kyoto 606-8502, Japan; shogo@kusastro.kyoto-u.ac.jp
[4] Tuorla Observatory, Department of Physics and Astronomy, University of Turku, FI-21500 Piikkiö, Finland; rareko@utu.fi
[5] Instituto de Astronomía, Universidad Autónoma de México, P.O. Box 439027, San Diego, CA 92143, USA; richer@astrosen.unam.mx
[6] Isaac Newton Group of Telescopes, Apartado 321, E-38700 Santa Cruz de La Palma, Spain; ovidiuv@ing.iac.es
[7] Instituto de Astronomía, Universidad Católica del Norte, Avenida Angamos 0610, Antofagasta, Chile
[8] ACRU & SAAO, University of KwaZulu-Natal, School of Mathematical Sciences, Durban 4041, South Africa
[9] Department of Astronomy, University of Cape Town, Rondebosch 7700, South Africa; pwoudt@ast.uct.ac.za
*Received 2009 March 27; accepted 2010 April 26; published 2010 May 21*

## ABSTRACT

We present deep near-infrared ($K_s$) images and surface photometry for 80 dwarf irregular galaxies (dIs) within ∼5 Mpc of the Milky Way. The galaxy images were obtained at five different facilities between 2004 and 2006. The image reductions and surface photometry have been performed using methods specifically designed for isolating faint galaxies from the high and varying near-infrared sky level. Fifty-four of the 80 dIs have surface brightness profiles which could be fit to a hyperbolic-secant (sech) function, while the remaining profiles could be fit to the sum of a sech and a Gaussian function. From these fits, we have measured central surface brightnesses, scale lengths, and integrated magnitudes. This survey is part of a larger study of the connection between large-scale structure and the global properties of dIs, the hypothesized building-blocks of more massive galaxies.

*Key words:* galaxies: dwarf – galaxies: fundamental parameters – galaxies: irregular – galaxies: photometry – infrared: galaxies – surveys

## 1. INTRODUCTION

In 1992, Schmidt and Boller investigated the three-dimensional distribution of nearly 300 galaxies with $v_{LG} < 500\,\mathrm{km\,s^{-1}}$. They concluded that the Local Group is part of a filamentary structure with a larger concentration of galaxies than the surrounding Local Supercluster (Schmidt & Boller 1992). This finding has been confirmed by more recent studies based on distance estimates with improved accuracy. For example, Peebles et al. (2001) describe the Local Group as part of an "...expanding filamentary structure, with the nearest big galaxies close to each other in the sky...." Similarly, Karachentsev et al. (2002) refer to the local galaxy distribution as "...rather inhomogeneous, showing concentration of the objects toward two opposite directions... which confirms the location of the Local Group in a filament, extending from Canes Venatici to Sculptor."

Among the types of galaxies which constitute our apparently fractalized Local Supercluster, dwarf irregulars (dIs), the suspected building-blocks of more massive galaxies, are by far the most plentiful in number. They therefore serve as ideal probes of the environment in which they evolved. Our location *within* a structure comprised mainly of dIs makes our local dIs especially useful for gaining insights into the evolution of structure on large scales. Furthermore, owing to the proximity of these galaxies, measurements of their properties can be made with high accuracy. Of particular interest is whether the global properties of dIs, such as their stellar mass and gas fraction, are affected by the cosmic structures in which they reside, as the "nature versus nurture" argument for dIs could be resolved by identifying environmental signatures in some dI diagnostics while not in others.

In order to establish whether the current arrangement of dIs is correlated with their global properties, we require reliable indicators of the mass components of a dI. Optical magnitudes are not trustworthy indicators of the stellar mass of a dI as they are often dominated by blue light from newborn O and B stars. In order to obtain measurements of mass-dependent properties of dIs with the accuracy necessary for statistically meaningful studies of their spatial distributions, it is necessary to observe dIs in the near-infrared (NIR). Vaduvescu et al. (2005) showed that more than 95% of a dI's light in $K_s$ (2.15 $\mu$m) can be attributed to stars older than ∼4 Gyr. Similarly, Cairós et al. (2003), Noeske et al. (2003), and Vaduvescu et al. (2007) have demonstrated for a large sample of blue compact dwarfs that the surface brightness profile (SBP) of a dI's underlying old stellar population can be investigated near its center owing to the lower contribution of the central starburst in the NIR compared to the optical. Thus, the NIR is well suited for tracing the old population dominating the stellar mass of a dI. Unfortunately, most dIs are too faint to have been detected by the Two Micron All Sky Survey (2MASS)[10] completed in 2001, and Kirby et al. (2008) show that the total magnitudes reported by 2MASS for low surface brightness galaxies can be underestimated by up to 2.5 mag. Furthermore, deeper NIR imaging surveys of dIs (e.g., Hunter & Elmegreen 2006) have not focused exclusively on nearby objects, leaving the majority of dIs within 5 Mpc of the Milky Way with unreliable mass estimates. We have therefore conducted an extensive $K_s$ imaging survey of nearby dIs for the

[10] This publication makes use of data products from the Two Micron All Sky Survey, which is a joint project of the University of Massachusetts and the Infrared Processing and Analysis Center/California Institute of Technology, funded by the National Aeronautics and Space Administration and the National Science Foundation.

purpose of establishing how the masses and mass-dependent properties of dIs are arranged locally.

This paper has been organized as follows. In Section 2, we summarize the criteria for inclusion in the $K_s$ imaging survey and present the observing log. In Section 3, we describe the image reduction procedure. In Section 4, we present the NIR surface and integrated photometry of the targets. The self-consistency of the photometric parameters is investigated by comparing the data for the targets observed at more than one facility. In Section 5, concluding statements are made about the objective of the survey and the reliability of the photometric data. In Paper II, we present the complete sample of dIs for which NIR photometry has been acquired and investigate connections between the global properties of dIs and their environment.

## 2. OBSERVATIONS

The NIR observations presented in this paper include all dIs (with the exception of the LMC and SMC) in the Local Volume catalog of Karachentsev et al. (2004) for which distance indicators place them within roughly ∼5 Mpc of the Milky Way, and for which deep $K_s$ surface photometry has not been obtained elsewhere. According to the rough completeness analysis of Karachentsev et al. (2004), the Local Volume survey is 70%–80% complete within 8 Mpc.

The $K_s$ imaging survey was conducted over eight observing runs between 2004 May and 2006 July. The runs were conducted at the 3.6 m Canada–France–Hawaii Telescope (CFHT), the 2.1 m telescope of the Observatorio Astronómico Nacional at San Pedro Martir (OAN-SPM), the Blanco 4 m telescope at the Cerro Tololo Inter-American Observatory (CTIO), the 3.6 m New Technology Telescope (NTT) operated by the European Southern Observatory (ESO) at La Silla, and the 1.4 m Infrared Survey Facility (IRSF) telescope hosted by the South African Astronomical Observatory (SAAO). Several galaxies have been observed at multiple facilities to check the pre-processing method used for each site, the quality of the sky subtraction, and the zero points computed for each image.

Obtaining deep images of dIs in the NIR poses several challenges which require great care to overcome in both the observing and reduction processes. Not only is the sky background high in the NIR, it also varies both spatially across the chip and temporally. Thus, the total on-target integration times must be split into sub-exposures, and the sky background must be repeatedly sampled close in time to each sub-exposure so that the sky pattern in each sub-exposure can be sufficiently subtracted.

The low surface brightnesses that are typical of dIs make it especially important to ensure that the low galaxy signal is not corrupted by inadequecies in the background determination. In their detailed analysis of NIR imaging strategies for faint extended sources, Vaduvescu & McCall (2004) found that at CFHT the mean brightness of the background signal in $K'$ (2.12 $\mu$m) varied on average by 0.5% per minute. Thus, to measure the sky pattern in each frame with a precision of at least 1%, we have followed the NIR observing guidelines of Vaduvescu & McCall (2004); namely, to chop between on-target and off-target positions with no more than 90 s between each pointing. Sets of 1 to 6 exposures were taken at each on-target position, and the pointings for each set of exposures were dithered by a few pixels to aid in the removal of detector artifacts. As recommended by Vaduvescu & McCall (2004), off-target positions were dithered by at least 20″ so that stars and distant galaxies could be removed. These star-subtracted images taken before and after each on-target exposure could then be used to interpolate an image of the sky pattern at the time of the on-target exposure (see Section 3.2).

The on-target observing sequences and exposure times are given in the facility-specific sections below. In cases where the galaxy was less than half the size of the detector field (in $B$), observing times were minimized by alternating the galaxy's position between halves or quadrants of the detector field. In this fashion, a reliable image of the galaxy's underlying sky pattern at each pointing could be obtained from the half or quadrant of the field that contained the galaxy in the previous pointing.

A log of our observations is provided in Table 1. The observing configurations at each facility are described in the sections below in chronological order. The sky was primarily photometric throughout the observing sequences for all of the detected galaxies except for at the CTIO and ESO, where the detected galaxies were all observed through thin clouds. This was accounted for by deriving the photometric zero point for each galaxy image from 2MASS stars on the galaxy image itself (see Section 3.3).

### 2.1. CFHT Observations

On the nights of February 23 and March 6–8 in 2004, we observed 27 survey targets with the 3.6 m CFHT atop Mauna Kea in Hawaii. The telescope was equipped with the CFHT-IR detector installed at the $f/8$ Cassagrain focus. The detector employs an HgCdTe 1024 × 1024 pixel array with a scale of 0.″211 pixel$^{-1}$, yielding a 3.′6 × 3.′6 field of view. All observations were made with the $K'$ filter. The individual exposure times for each galaxy were 75 s for a total on-target integration time of 10 minutes. Of the 27 galaxies observed, only KK98–208 was not detected.

### 2.2. OAN-SPM Observations

In March and April of 2005, we observed 11 survey targets over the course of seven nights with the 2.1 m telescope at OAN-SPM in Baja California, Mexico. The CAMILA NIR camera contains a NICMOS3 256 × 256 pixel array installed at the $f/13.5$ Cassegrain focus (see Cruz-González et al. 1994). The pixel scale is 0.″85 pixel$^{-1}$, resulting in a 3.′6 × 3.′6 field of view. All observations were made with the $K'$ filter. Individual on-target exposures times were typically 60 s for a total of 40 minutes per galaxy. Of the 11 targets observed, E443–09 and KKR25 could not be detected sufficiently well for photometry to be obtained.

### 2.3. IRSF Observations

Over the course of seven nights in June and July of 2005 and six nights in July of 2006, we observed 26 survey targets with the 1.4 m IRSF, a joint Japanese/South African facility located at the SAAO near Sutherland, South Africa. The IRSF employs the Simultaneous-3color InfraRed Imager for Unbiased Survey (SIRIUS), which consists of three 1024 × 1024 HgCdTe arrays for simultaneous observing in the $J$ (1.25 $\mu$m), $H$ (1.63 $\mu$m), and $K_s$ filters. The field of view is 7.′7 × 7.′7 with a pixel scale of 0.″45 pixel$^{-1}$. On-target integration times were typically between 40 and 100 minutes of 30 s exposures. Only KK98–196 and P51659 could not be detected sufficiently well for photometry to be obtained.

### 2.4. CTIO Observations

In July of 2006, we were granted two nights with the Blanco 4 m telescope at the CTIO in Chile. The telescope was equipped

**Table 1**
Observations

| Galaxy | Instrument | Date (UT) | Exposure Time (s) | Image Size (arcmin) | FWHM (arcsec) |
|---|---|---|---|---|---|
| ANTLIA | SPM-CAMILA | 2005 Apr 24 | 2400 | 2.8 × 2.8 | 4.2 |
| CAMB | CFHT-IR | 2004 Mar 7 | 600 | 3.2 × 3.2 | 1.9 |
| CAS1 | CFHT-WIRCAM | 2006 Jul 11 | 1140 | 8.0 × 8.0 | 3.3 |
| CGCG087-33 | SPM-CAMILA | 2005 Apr 21 | 2400 | 2.8 × 2.8 | 2.2 |
| DDO120 | CFHT-IR | 2004 Mar 8 | 600 | 3.2 × 3.2 | 0.6 |
| DDO122 | CFHT-IR | 2004 Mar 8 | 600 | 3.2 × 3.2 | 1.2 |
| DDO125 | CFHT-IR | 2004 Mar 7 | 600 | 3.2 × 3.2 | 1.3 |
| DDO165 | CFHT-IR | 2004 Mar 8 | 600 | 3.2 × 3.2 | 1.2 |
| DDO168 | CFHT-IR | 2004 Mar 7 | 600 | 3.2 × 3.2 | 1.3 |
| DDO169 | CFHT-IR | 2004 Mar 8 | 600 | 3.2 × 3.2 | 1.4 |
| DDO181 | CFHT-IR | 2004 Mar 8 | 600 | 3.2 × 3.2 | 0.7 |
| DDO190 | CFHT-IR | 2004 Mar 8 | 600 | 3.2 × 3.2 | 1.3 |
| DDO210 | CFHT-WIRCAM | 2006 May 19 | 1020 | 8.0 × 8.0 | 3.1 |
| DDO226 | IRSF-SIRIUS | 2006 Jun 10 | 4320 | 6.9 × 6.9 | 2.9 |
| DDO43 | CFHT-IR | 2004 Feb 24 | 600 | 3.2 × 3.2 | 1.1 |
| DDO46 | CFHT-IR | 2004 Mar 7 | 600 | 3.2 × 3.2 | 1.0 |
| DDO52 | CFHT-IR | 2004 Feb 24 | 600 | 3.2 × 3.2 | 1.2 |
| DDO53 | CFHT-WIRCAM | 2005 Dec 13 | 955 | 8.0 × 8.0 | 3.0 |
| DDO6 | IRSF-SIRIUS | 2006 Jun 9 | 4500 | 3.0 × 3.0 | 2.3 |
| DDO6 | NTT-SOFI | 2006 Jul 2 | 2640 | 4.6 × 4.6 | 1.5 |
| DDO87 | CFHT-IR | 2004 Mar 7 | 1200 | 3.2 × 3.2 | 1.1 |
| DDO99 | CFHT-IR | 2004 Mar 8 | 600 | 3.2 × 3.2 | 1.5 |
| DW2 | CFHT-WIRCAM | 2005 Nov 18 | 959 | 8.0 × 8.0 | 2.1 |
| E215-09 | IRSF-SIRIUS | 2005 May 16 | 2070 | 3.0 × 3.0 | 2.9 |
| E269-58 | IRSF-SIRIUS | 2006 Jun 11 | 4320 | 6.9 × 6.9 | 1.6 |
| E321-14 | IRSF-SIRIUS | 2005 May 16 | 2070 | 3.0 × 3.0 | 2.1 |
| E324-24 | IRSF-SIRIUS | 2005 Jun 2 | 4140 | 3.0 × 3.0 | 2.1 |
| E325-11 | IRSF-SIRIUS | 2006 Jun 9 | 4320 | 6.9 × 6.9 | 2.1 |
| E325-11 | CTIO-ISPI | 2006 Jul 15 | 1020 | 9.7 × 9.7 | 2.6 |
| E349-31 | IRSF-SIRIUS | 2006 Jun 7 | 9000 | 3.0 × 3.0 | 2.2 |
| E349-31 | NTT-SOFI | 2006 Jul 2 | 2640 | 4.6 × 4.6 | 3.0 |
| E379-07 | IRSF-SIRIUS | 2005 May 16 | 6210 | 3.0 × 3.0 | 2.0 |
| E381-18 | IRSF-SIRIUS | 2005 May 16 | 2520 | 3.0 × 3.0 | 2.3 |
| E381-20 | CTIO-ISPI | 2006 Jul 15 | 1800 | 9.7 × 9.7 | 2.6 |
| E384-16 | IRSF-SIRIUS | 2005 Jun 6 | 1530 | 3.0 × 3.0 | 2.2 |
| E443-09 | SPM-CAMILA | 2005 Mar 23 | 2820 | ... | ... |
| E444-78 | CFHT-IR | 2004 Mar 7 | 600 | 3.2 × 3.2 | 1.5 |
| E444-84 | CFHT-IR | 2004 Mar 8 | 600 | 3.2 × 3.2 | 1.5 |
| HIDEEPJ1337-33 | NTT-SOFI | 2006 Jul 2 | 1380 | ... | ... |
| HIPASSJ1247-77 | IRSF-SIRIUS | 2006 Jun 8 | 6750 | 3.0 × 3.0 | 2.0 |
| HIPASSJ1247-77 | NTT-SOFI | 2006 Jul 2 | 2580 | 2.2 × 2.2 | 1.5 |
| HIPASSJ1337-39 | NTT-SOFI | 2006 Jul 2 | 2580 | 2.2 × 2.2 | 1.5 |
| HIPASSJ1348-37 | IRSF-SIRIUS | 2006 Jun 9 | 6750 | 3.0 × 3.0 | 2.1 |
| HIPASSJ1351-47 | IRSF-SIRIUS | 2006 Jun 7 | 6750 | 3.0 × 3.0 | 2.1 |
| HOI | CFHT-WIRCAM | 2005 Dec 10 | 840 | 8.0 × 8.0 | 2.9 |
| I3104 | IRSF-SIRIUS | 2006 Jun 10 | 4320 | 6.9 × 6.9 | 1.5 |
| I3687 | CFHT-IR | 2004 Mar 8 | 600 | 3.2 × 3.2 | 1.2 |
| I4182 | CFHT-WIRCAM | 2006 Jul 9 | 960 | 8.0 × 8.0 | 2.5 |
| I4247 | SPM-CAMILA | 2005 Apr 20 | 2220 | 2.8 × 2.8 | 2.4 |
| I4316 | SPM-CAMILA | 2005 Apr 21 | 2160 | 2.8 × 2.8 | 2.4 |
| I4662 | IRSF-SIRIUS | 2006 Jun 6 | 4320 | 6.9 × 6.9 | 1.6 |
| I5152 | IRSF-SIRIUS | 2006 Jun 8 | 4320 | 6.9 × 6.9 | 1.2 |
| KDG52 | CFHT-WIRCAM | 2005 Dec 13 | 956 | 8.0 × 8.0 | 3.0 |
| KK17 | CFHT-WIRCAM | 2006 Jan 20 | 740 | 8.0 × 8.0 | 2.9 |
| KK182 | IRSF-SIRIUS | 2006 Jun 6 | 4500 | 3.0 × 3.0 | 2.2 |
| KK182 | NTT-SOFI | 2006 Jul 2 | 2580 | 2.2 × 2.2 | 1.5 |
| KK195 | IRSF-SIRIUS | 2006 Jun 7 | 6750 | 3.0 × 3.0 | 2.2 |
| KK196 | IRSF-SIRIUS | 2005 May 31 | 1530 | ... | ... |
| KK208 | CFHT-IR | 2004 Mar 8 | 600 | ... | ... |
| KK230 | CFHT-WIRCAM | 2006 Jul 9 | 1200 | 8.0 × 8.0 | 2.8 |
| KKH11 | CFHT-IR | 2004 Mar 8 | 600 | 3.2 × 3.2 | 1.2 |
| KKH12 | CFHT-WIRCAM | 2005 Dec 9 | 980 | 8.0 × 8.0 | 2.7 |
| KKH6 | CFHT-WIRCAM | 2006 Jul 11 | 960 | 6.0 × 6.0 | 4.8 |
| KKH60 | IRSF-SIRIUS | 2006 Jun 9 | 6750 | 3.0 × 3.0 | 3.9 |
| KKH86 | IRSF-SIRIUS | 2006 Jun 8 | 6750 | 3.0 × 3.0 | 2.1 |
| KKH98 | CFHT-WIRCAM | 2006 Jan 17 | 750 | 8.0 × 8.0 | 2.7 |

**Table 1**
(Continued)

| Galaxy | Instrument | Date (UT) | Exposure Time (s) | Image Size (arcmin) | FWHM (arcsec) |
|---|---|---|---|---|---|
| KKR25 | SPM-CAMILA | 2005 Apr 21 | 4800 | ... | ... |
| N4523 | CFHT-IR | 2004 Mar 7 | 600 | 3.2 × 3.2 | 1.1 |
| P45628 | SPM-CAMILA | 2005 Mar 21 | 2340 | 2.8 × 2.8 | 2.9 |
| P47885 | NTT-SOFI | 2006 Jul 2 | 2580 | 2.2 × 2.2 | 1.1 |
| P51659 | IRSF-SIRIUS | 2006 Jun 6 | 4320 | ... | ... |
| PEGDIG | CFHT-WIRCAM | 2006 Jan 17 | 965 | 8.0 × 8.0 | 2.7 |
| SAGDIG | CFHT-WIRCAM | 2006 May 11 | 960 | 8.0 × 8.0 | 2.9 |
| SEXA | IRSF-SIRIUS | 2006 Jun 7 | 4320 | 6.9 × 6.9 | 2.2 |
| SEXA | CTIO-ISPI | 2006 Jul 14 | 1680 | 9.7 × 9.7 | 2.5 |
| SEXB | IRSF-SIRIUS | 2005 May 20 | 990 | 6.9 × 6.9 | 2.3 |
| U2684 | CFHT-IR | 2004 Feb 24 | 600 | 3.2 × 3.2 | 1.1 |
| U3755 | SPM-CAMILA | 2005 Apr 19 | 2340 | 2.8 × 2.8 | 2.1 |
| U3817 | CFHT-IR | 2004 Mar 8 | 600 | 3.2 × 3.2 | 1.1 |
| U4483 | CFHT-IR | 2004 Feb 24 | 525 | 3.2 × 3.2 | 1.6 |
| U5288 | CFHT-WIRCAM | 2006 Jan 19 | 910 | 8.0 × 8.0 | 1.6 |
| U5423 | CFHT-IR | 2004 Mar 7 | 525 | 3.2 × 3.2 | 0.9 |
| U5829 | CFHT-IR | 2004 Mar 8 | 600 | 3.2 × 3.2 | 1.3 |
| U7298 | SPM-CAMILA | 2005 Apr 25 | 2400 | 2.8 × 2.8 | 3.1 |
| U7559 | CFHT-IR | 2004 Mar 8 | 600 | 3.2 × 3.2 | 1.9 |
| U7605 | CFHT-WIRCAM | 2006 Jul 13 | 1200 | 8.0 × 8.0 | 2.8 |
| U8638 | SPM-CAMILA | 2005 Apr 25 | 2400 | 2.8 × 2.8 | 2.1 |
| U8833 | SPM-CAMILA | 2005 Apr 20 | 2400 | 2.8 × 2.8 | 0.9 |
| UA292 | CFHT-WIRCAM | 2006 Jul 12 | 960 | 8.0 × 8.0 | 2.2 |
| UA319 | CFHT-IR | 2004 Mar 7 | 600 | 3.2 × 3.2 | 1.0 |
| UA438 | IRSF-SIRIUS | 2006 Jun 7 | 4500 | 3.0 × 3.0 | 2.4 |
| UA438 | NTT-SOFI | 2006 Jul 2 | 2640 | 4.6 × 4.6 | 1.0 |
| UA86 | CFHT-WIRCAM | 2006 Jan 18 | 689 | 8.0 × 8.0 | 1.6 |

with the Infrared Side-Port Imager (ISPI) mounted at the $f/8$ Cassagrain focus. The camera uses a Hawaii 2048 × 2048 pixel array with a scale of $0\farcs3$ pixel$^{-1}$ and a $10\farcm25 \times 10\farcm25$ field of view. Each target was observed using sequences of either three co-added 20 s exposures or six co-added 10 s exposures, with total on-target integration times of approximately 30 minutes. All observations were made with the $K_s$ filter. The first night was clouded out, and due to lengthy cloudy periods on the second night, we were only able to obtain complete observing sequences for three survey targets.

### 2.5. ESO Observations

On the night of 2006 July 2, we observed eight survey targets with the 3.6 m NTT at the ESO at La Silla, Chile. The SofI (Son of ISAAC) infrared spectrograph and imaging camera was installed at the Nasmyth A focus. SofI consists of a Hawaii HgCdTe 1024 × 1024 pixel array with a scale of $0\farcs288$ pixel$^{-1}$ and a $4\farcm92 \times 4\farcm92$ field of view. Each target was observed with sequences of six co-added 10 s exposures for a total on-target integration time of approximately 45 minutes. Only HIDEEPJ1337–33 could not be detected sufficiently well for photometry to be obtained.

### 2.6. WIRCam Observations

During the 2005B and 2006A semesters, we obtained $K_s$ images of 18 targets via Queued Service Observing (QSO) with the Wide-Field IR Camera (WIRCam) installed on the 3.6 m CFHT. WIRCam contains four 2048 × 2048 pixel HAWAII2-RG detectors spanning a $20' \times 20'$ field of view with a sampling of $0\farcs3$ pixel$^{-1}$. Each target was observed for at least one 16 minute sequence consisting of 20 s exposures with the target alternately positioned within each of the four $10' \times 10'$ arrays. Thus, sky images could be produced using the three galaxy-free fields.

## 3. IMAGE REDUCTION

Given the diversity of the facilities used in this imaging survey, great care has been taken throughout the reduction process to insure that all photometric data are self-consistent. The image reductions for all of the dIs we have observed have been performed using methods specially designed for isolating faint galaxies from the high NIR sky level, which varies significantly from site to site. The methods employed are described in the following paragraphs. The reduced galaxy images are presented in Figure 1.

### 3.1. Image Preprocessing

Our image reduction sequence follows the recommendations of Vaduvescu & McCall (2004) and is described in detail below. The first stage of the reduction process was to correct each sky and target exposure for bad pixels. Bad pixel maps were built for each run, excluding WIRCam, by comparing pairs of flat-field images taken with two different exposure times. The maps were then applied to each exposure using the IRAF[11] *fixpix* task. For the WIRCam run in the 2005B semester, we adopted the QSO bad pixel mask that had been constructed closest in time to our observations. For the WIRCam run in the 2006A semester, we accepted the images that had been cleaned of detector imprints and flat-fielded by the WIRCam QSO pre-processing pipeline (not available for the 2005B semester).

Next, each exposure was divided by a flat field produced on the night of the observation. All flat fields were produced from a sequence of equal exposures of the darkening (or brightening) twilight sky. A flat field image could then be produced which

[11] IRAF is distributed by the National Optical Astronomy Observatory, which is operated by the Association of Universities for Research in Astronomy (AURA) under cooperative agreement with the National Science Foundation.

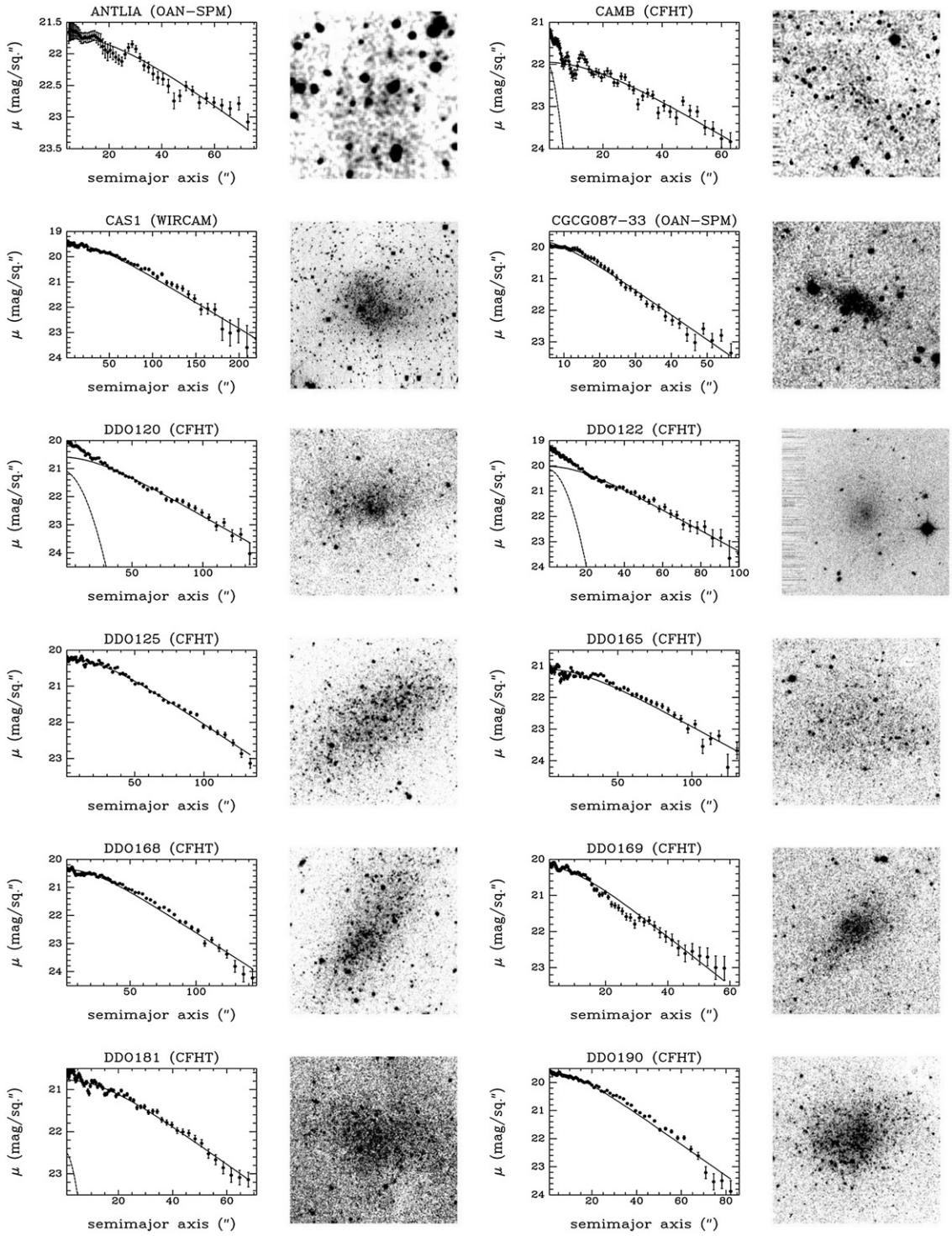


**Figure 1.** Left panels: SBPs in $K_s$. The solid line represents the sech fit to the profile. In cases where we obtained a better fit to the profile using the sum of a sech and a Gaussian function, the Gaussian fit is shown by a dashed line. Right panels: $K_s$ image of each detected galaxy, with the adopted galaxy centroid at the center of each frame. (north is up, east is to the left; image size is given in Table 1). Note: in the CTIO-ISPI image of E381-20, the extended signal that appears to the west of the galaxy is a defect caused by the saturated star to the east of the galaxy.

consisted of the relative sensitivity of each pixel, quantified by the slope of the linear fit to the pixel value versus the image mean over the course of the twilight sequence. This algorithm was implemented with the MAKEFLAT IDL routine written by Olivier Lai.[12] Again, for the WIRCam run in 2005, we adopted the QSO flat field that had been constructed closest in time to our observations. For the WIRCam run in 2006, flat fielding was applied by the WIRCam pre-processing pipeline, as explained above. The flat-fielded images therefore contain the bias and dark current, but these instrumental signatures are removed during the sky-subtraction process, as indicated below.

[12] CFHT Corporation, 65-1238 Mamalahoa Highway, Kamuela, HI 96743 USA; lai@cfht.hawaii.edu

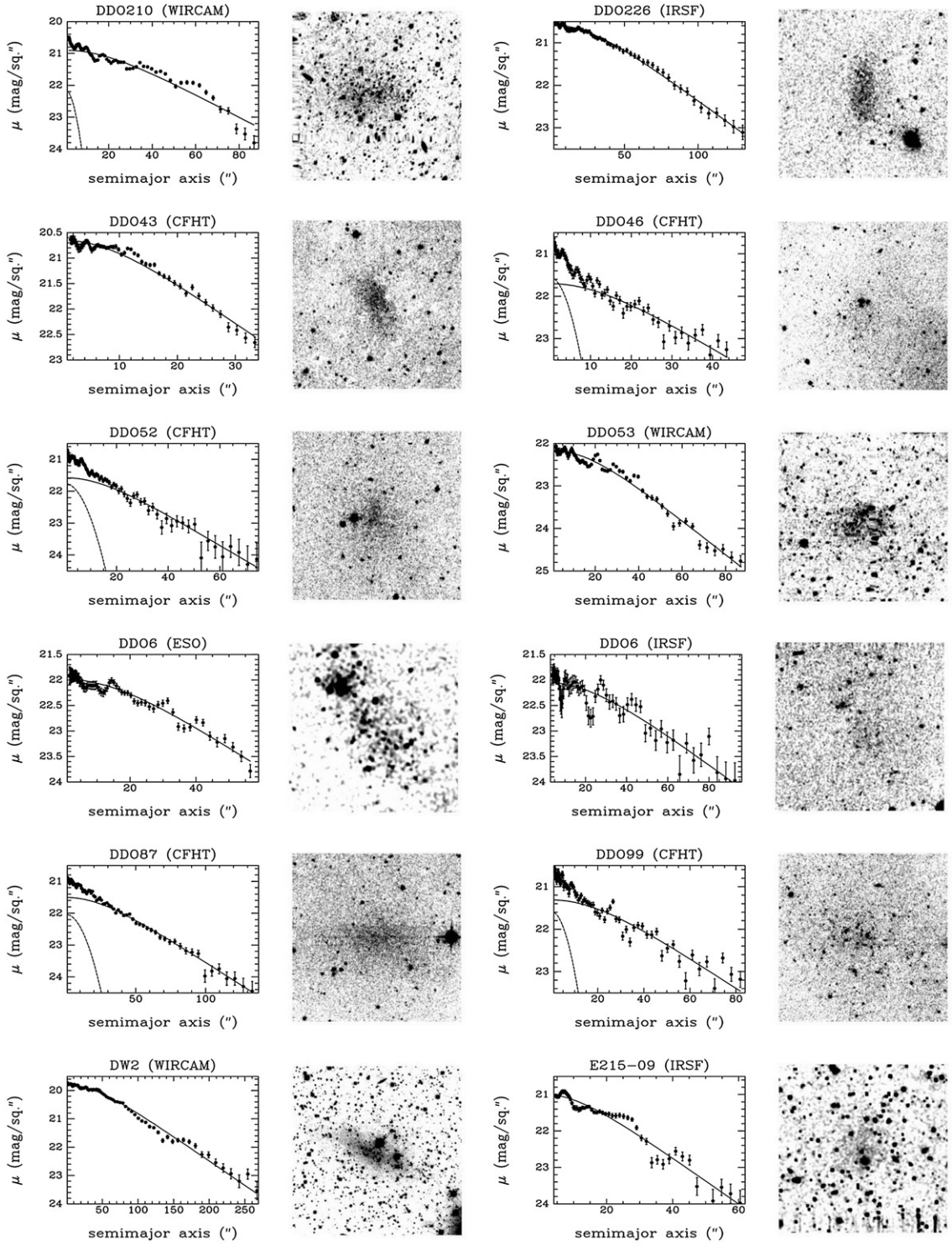


**Figure 1.** (Continued)

### *3.2. Sky Subtraction*

As explained in Section 2, the low surface brightness typical of dIs necessitates that the subtraction of the sky pattern from each galaxy exposure be accomplished using a sky image which closely represents the sky pattern at the time of each galaxy exposure. This has been accomplished with an IRAF script which takes a set of exposures following a sky-galaxy-sky sequence and creates an interpolated sky image from the sky exposures taken before and after each galaxy exposure. Specifically, each pair of dithered sky exposures was leveled to the average of their statistical modes, then subtracted from each other to reveal their stars and extended sources. These objects were then masked using IRAF's *objmask* task, taking care to select the masking parameters which best reflect the seeing and signal-to-noise ratio. Next, the masks were used to replace the stars and extended sources with the underlying sky signal obtained from the other dithered, leveled sky exposure, resulting in star-free images of the sky pattern immediately before and after the galaxy exposure. The two images were then averaged

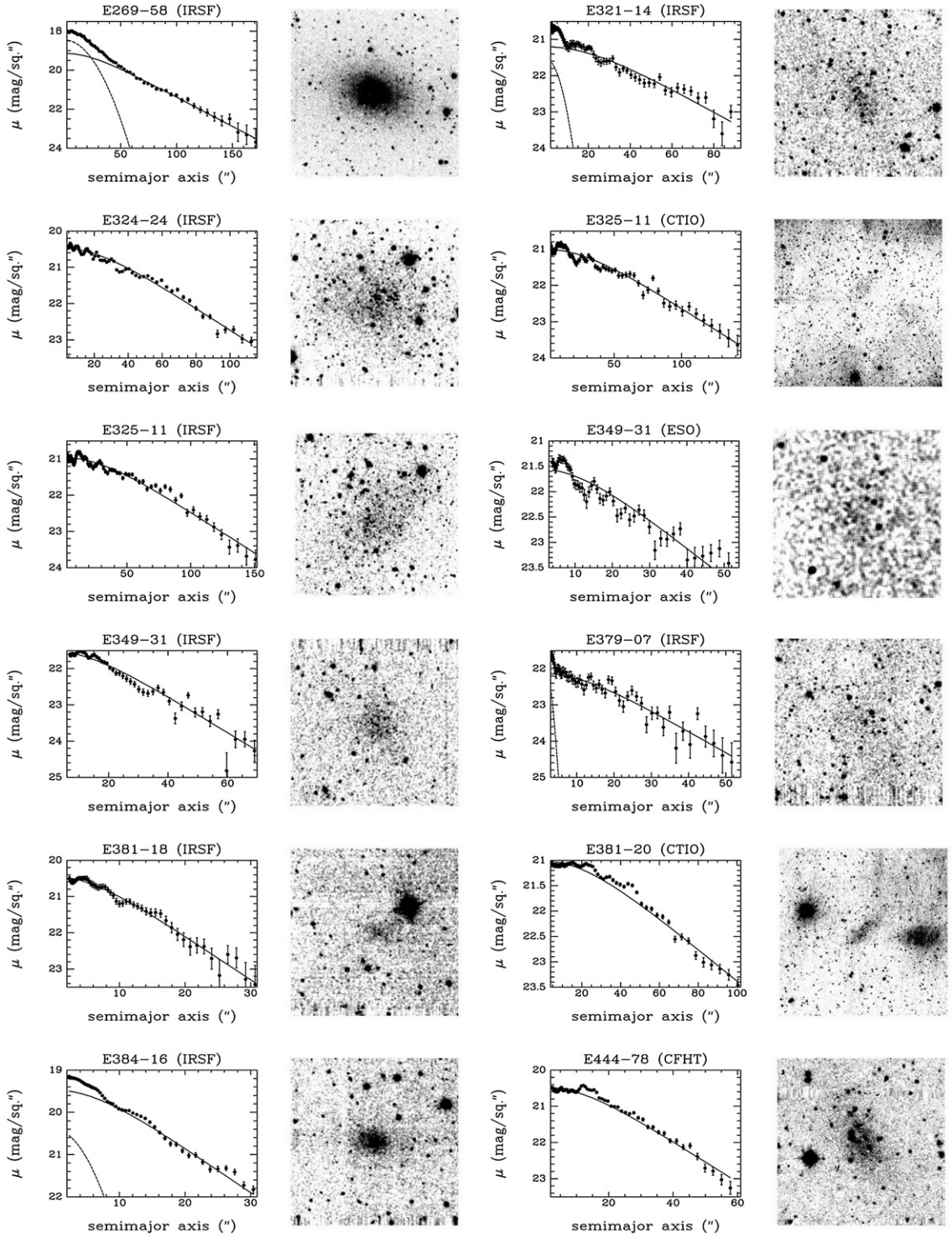


**Figure 1.** (Continued)

into a sky image which approximates the underlying sky pattern on the galaxy exposure. The final sky image contains the same instrumental signatures as the galaxy exposure, which means that the bias and dark current are removed from each galaxy image when the set of sky images is subtracted from the set of galaxy images. A final galaxy image could then be produced by aligning and combining the individual sky-subtracted galaxy images.

Despite our efforts to sample the sky frequently enough and long enough to overcome rapid variability of the NIR background, it is impossible to obtain a perfect match to a galaxy's underlying sky pattern. As a result, background residuals can occasionally be seen in the sky-subtracted images presented in Figure 1. We have accounted for these residuals by estimating the uncertainty in a galaxy's outermost isophotes owing to background residuals and incorporating this estimate into the uncertainties in the photometric parameters. This is described in more detail in Section 4.2.2. Many of the galaxy images also display some shallow negative residuals, which are a result of imperfect removal of stars from the sky images.

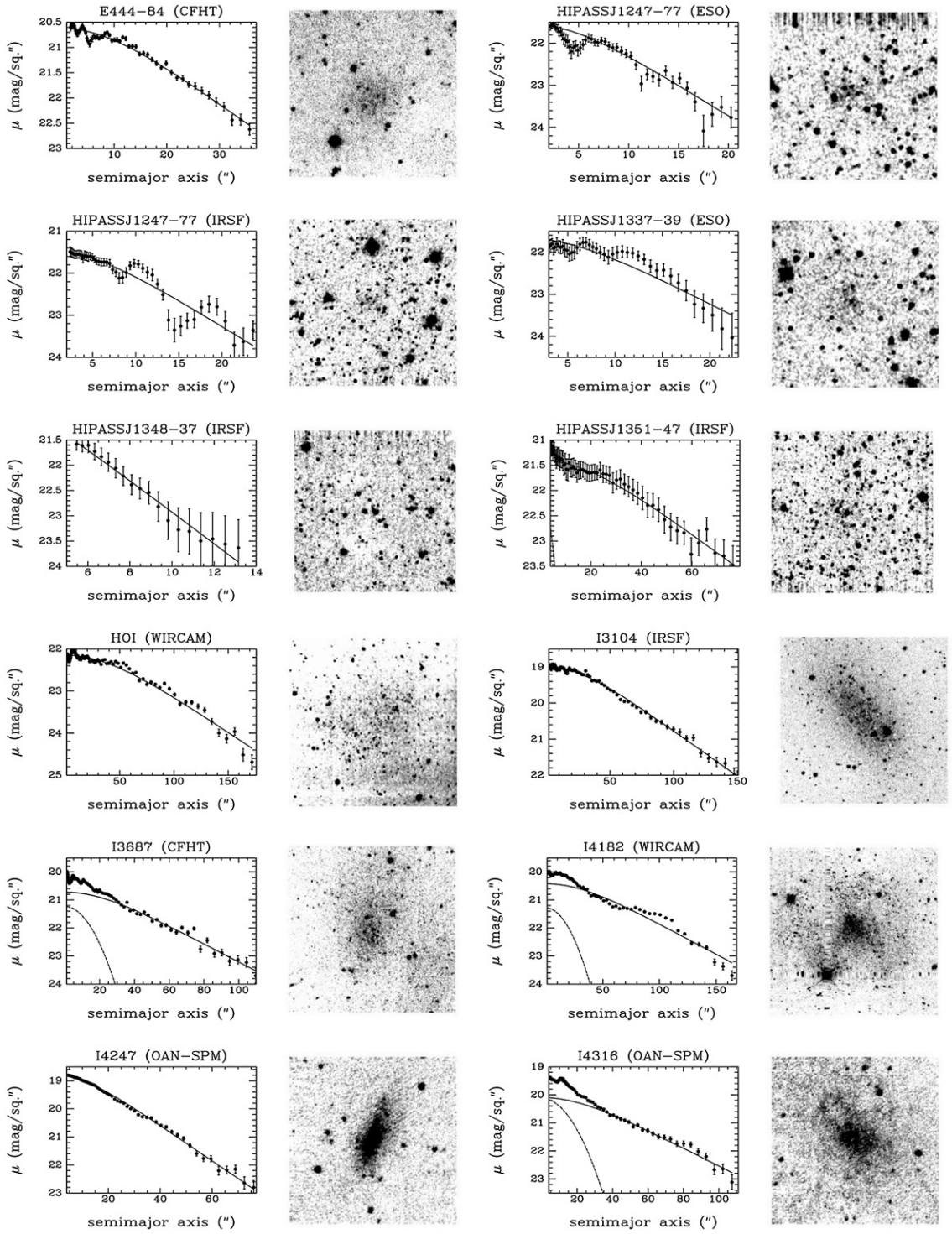


**Figure 1.** (Continued)

As explained in Section 4.1, these negative stellar residuals are masked prior to producing a galaxy's SBP.

### *3.3. Photometric Calibration*

Using IRAF's *ccxymatch* task, the stars in each galaxy field were matched with stars in the 2MASS Point Source Catalogue (PSC) with 2MASS photometric quality flags of either A or B (i.e., with photometric measurement uncertainties $\leqslant$0.15). The number of matched stars was typically between 3 and 20. The photometric zero point for each galaxy field was then computed from the average difference between the instrumental and 2MASS magnitudes, for which the rms was typically $\sim$0.1 mag. We were able to drop the color term owing to the fact that Vaduvescu et al. (2005) found that a remarkably constant $J - K_s$ color of 0.8–1.0 mag among 34 dIs and the mean $J - K_s$ color of the 2000 2MASS stars in our survey fields were $0.8 \pm 0.2$ mag. Five galaxy fields (DDO120, DDO122, DDO169, DDO181, and U7559) contained less than three 2MASS stars. Since all of these galaxies were observed

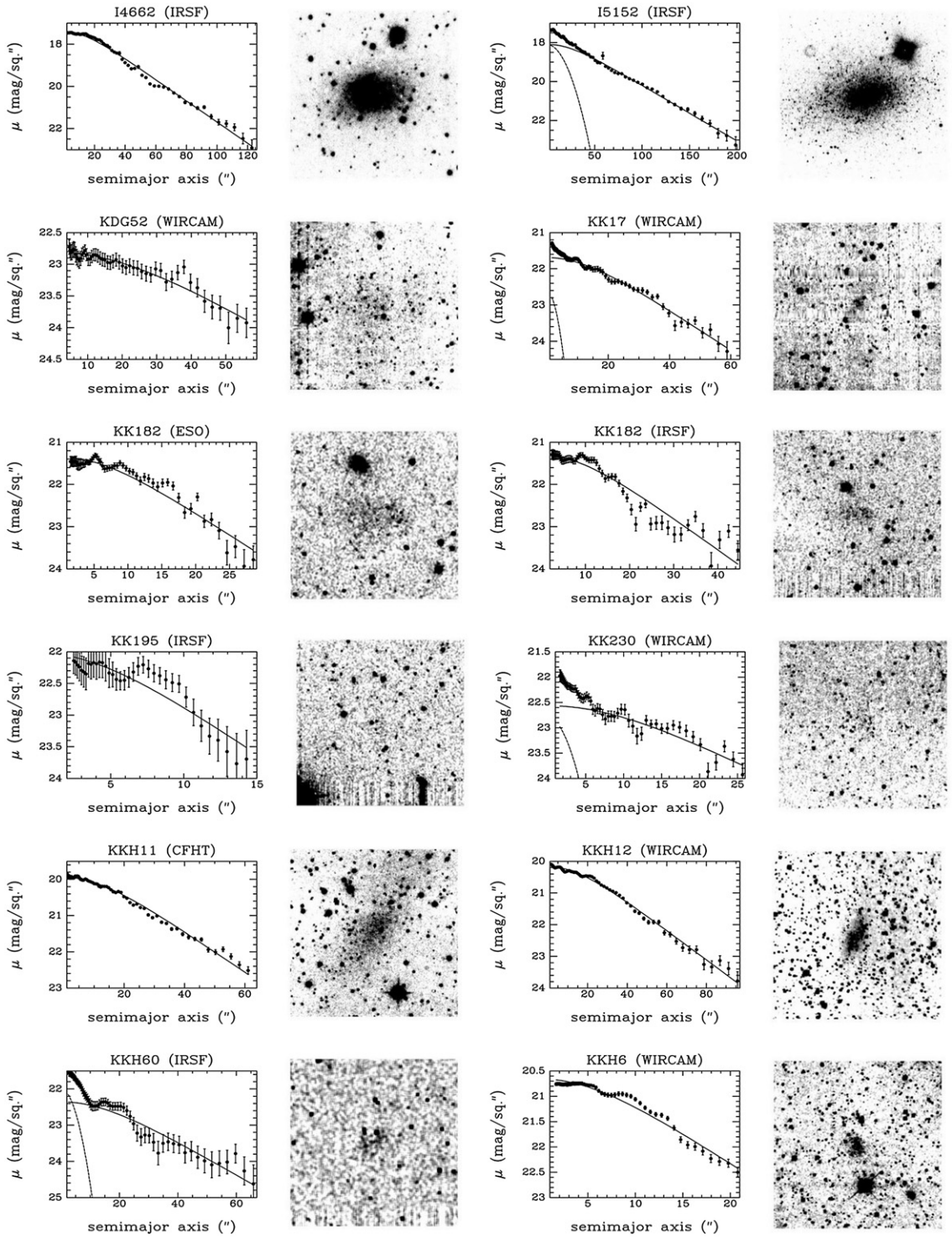


**Figure 1.** (Continued)

on the photometric night of 2004 March 8, their zero points could be estimated by interpolating, to the desired airmass, the zero points measured for the galaxies observed on the same night. The zero points were generally steady throughout each run, varying by only 0.1 mag with the CFHT-IR, 0.1 mag with the IRSF, 0.2 mag with SPM-CAMILA, 0.1 mag with the CTIO-ISPI, 0.4 mag with the NTT-SOFI, and 0.2 mag with WIRCam.

## 4. THE DATA

### *4.1. Surface Photometry*

In the NIR, dIs generally display regular elliptical morphologies without significant contamination from starburst emission (essentially by definition). The validity of adopting an elliptical isophotal model for dIs has been demonstrated by Vaduvescu

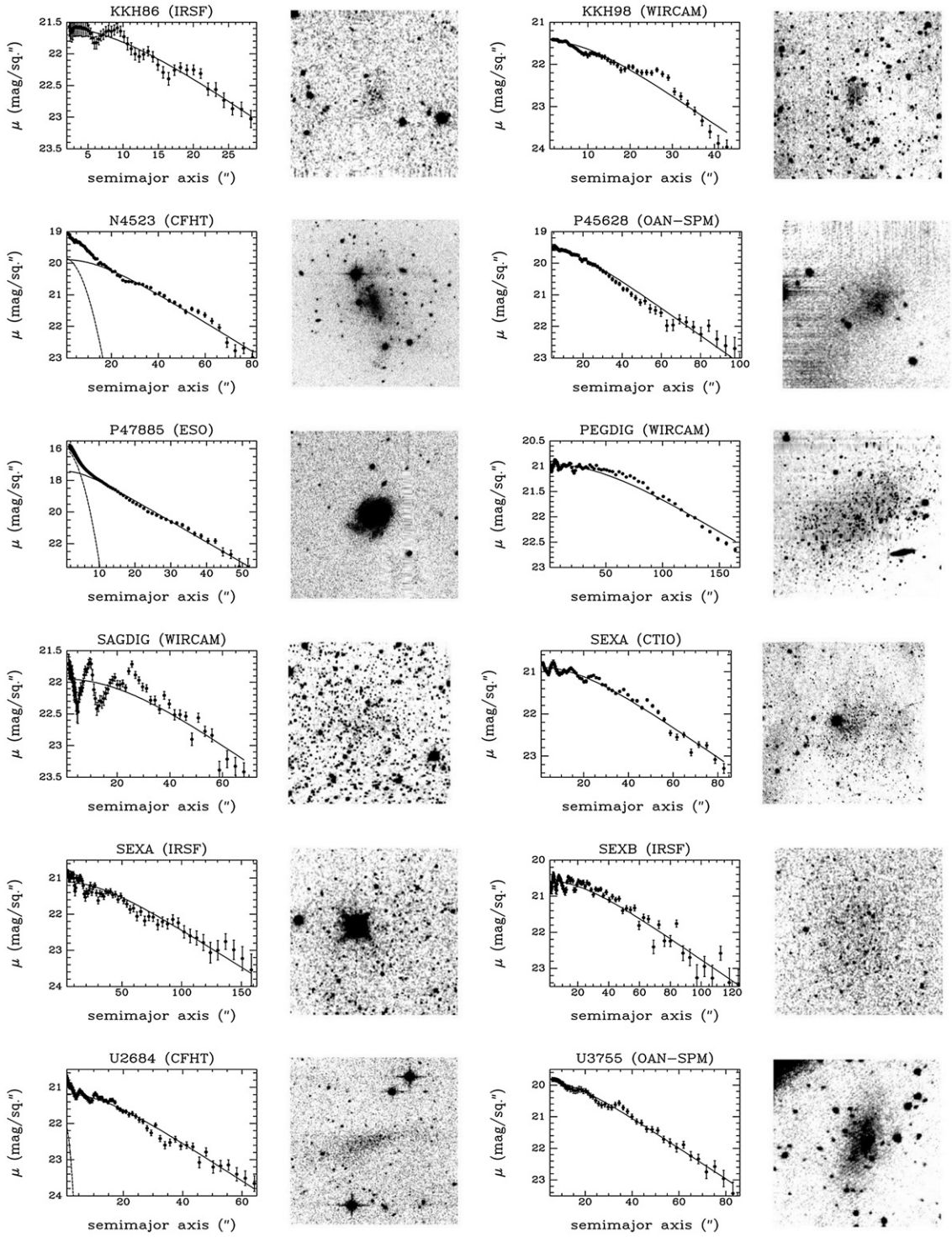


**Figure 1.** (Continued)

et al. (2005). In their NIR imaging survey of 34 dIs in the Local Volume, they found that a dI's total flux enclosed within its faintest elliptical isophote agrees closely with the total flux of the dI's diffuse component enclosed within the same isophote. Thus, deviations from an elliptical isophotal model due to recent star formation are not significant. Specifically, their study of the dIs' resolved components revealed that more than 95% of a dI's light in $K_s$ comes from stars older than ∼4 Gyr. Furthermore, they found that the total flux of each dI agrees closely with the flux obtained by integrating the fit to the galaxy's SBP, which was generated from elliptical isophotes of increasing size. The SBP of a dI can therefore be characterized by a global centroid, ellipticity and axis ratio. We have identified these parameters and constructed the SBPs for the dIs in this survey using the STSDAS IRAF *ellipse* task. Prior to applying the task, many of the galaxy images were binned so that each galaxy's shape and centroid could be reliably identified. Typical binning dimensions were $4 \times 4$ pixel ($0\farcs8 \times 0\farcs8$) for the CFHT-IR images, $4 \times 4$ pixel ($1\farcs8 \times 1\farcs8$) for the IRSF images, $8 \times 8$ pixel ($2\farcs4 \times 2\farcs4$) for the WIRCam images due to the noisy background, and no binning

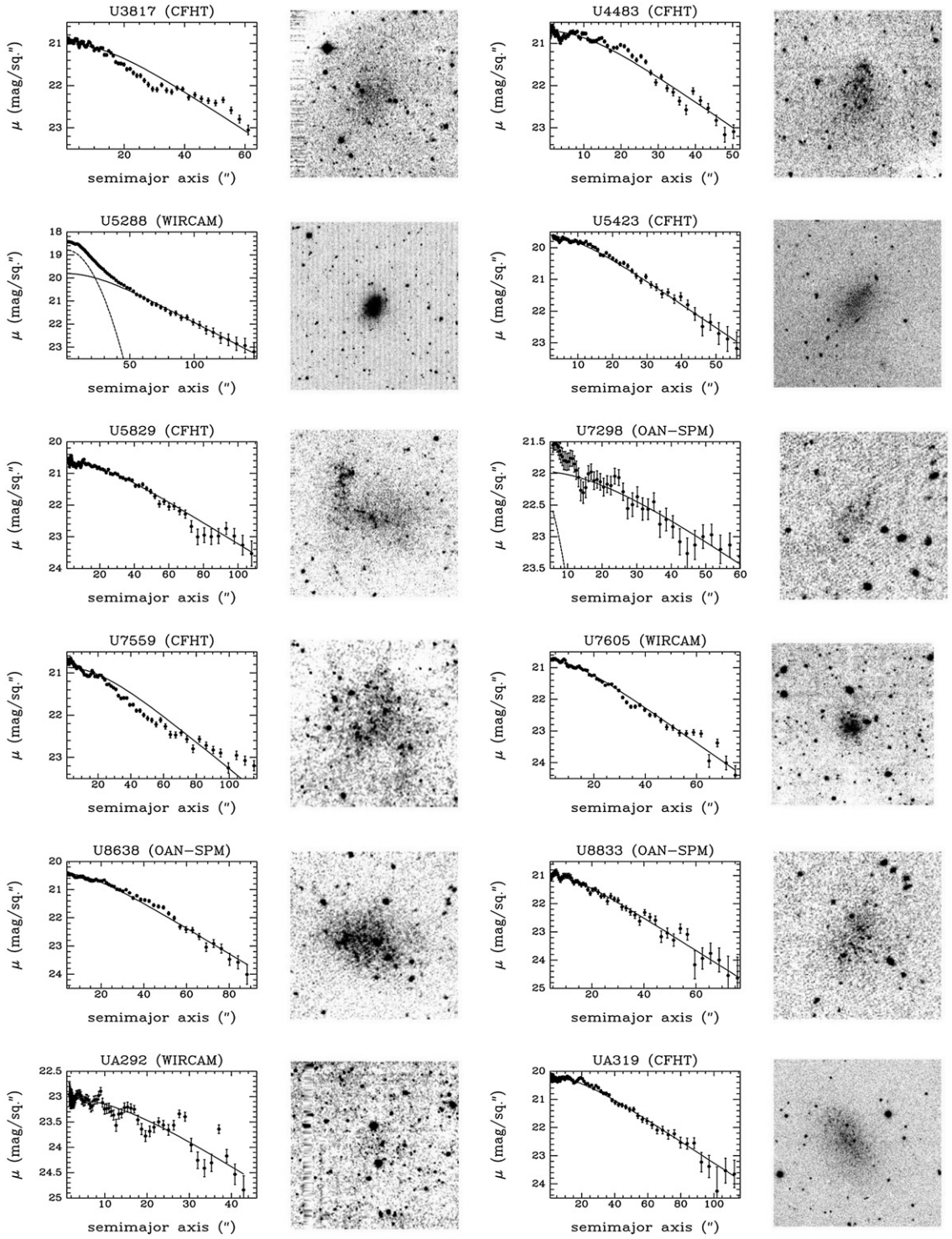


**Figure 1.** (Continued)

for the SPM-CAMILA, CTIO-ISPI, and NTT-SOFI images. To avoid contamination from resolved sources as well as from negative stellar residuals rising from imperfect sky subtraction (see Section 3.2), IRAF's *objmask* task was used to produce a mask of all resolved stars, small extended sources, and negative stellar residuals in the galaxy field. By associating each galaxy image with its mask, the *ellipse* task ignores the masked pixels when summing the intensities within each isophote.

For each galaxy, an initial estimate of its centroid, position angle ($\phi$), and ellipticity ($e$) was obtained by approximating, through visual inspection, the galaxy's elliptical extent. These parameters were then used with the *ellipse* task to produce a first approximation of the galaxy's SBP with the centroid allowed to vary freely with radius but the position angle and ellipticity held fixed. Next, the variation in the centroid with radius was examined in order to estimate the coordinates which best centered the outermost isophotes, where the old stellar population dominates the NIR light and therefore most clearly reveals the geometry of the entire galaxy. The centroid, ellipticity, and position angle were then fixed and the fitting

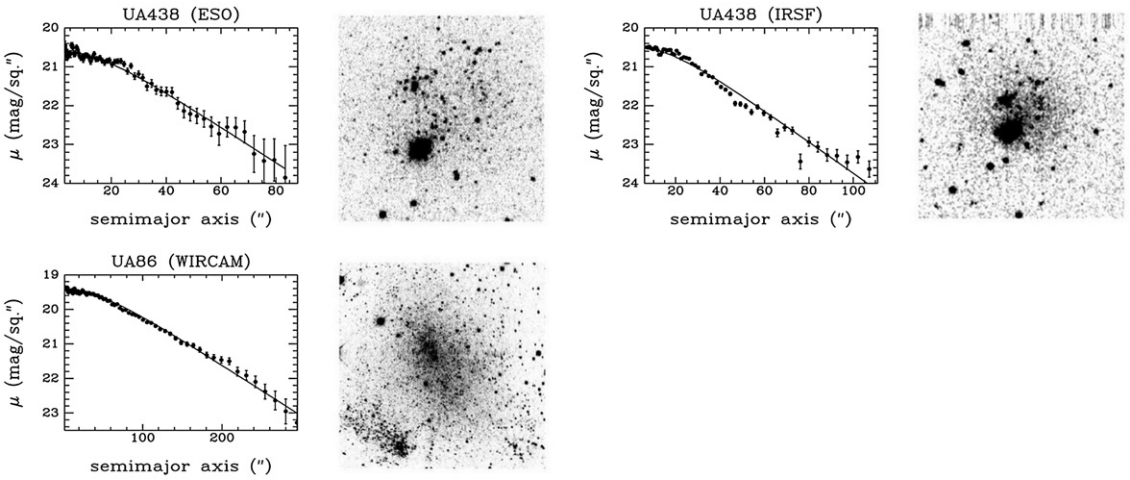


**Figure 1.** (Continued)

process was repeated. During this second stage, *ellipse* was run iteratively with a range of coordinates within ∼5″ of the estimate of the centroid from the outermost isophotes. In this manner, it was possible to identify the centroid for which elliptical isophotes could be identified down to intensity levels comparable to the noise of the sky background. Once the centroid of the light profile was established, the centroid was held fixed while the position angle and then the ellipticity were estimated by following the same iterative fitting process. The final SBP was produced by running *ellipse* with all three elliptical parameters fixed. In all runs of the *ellipse* task, we used geometric sampling along the semimajor axis to boost the signal-to-noise ratio of the outermost isophotes.

The parameters which were found to best characterize the elliptical profile of each galaxy are presented in Table 2. Uncertainties in the profile centroids, ellipticities, and position angles were computed by *ellipse* from the errors in the coefficients of each elliptical fit. These uncertainties were typically 0.″7, 2%, and 5% for the centroids, ellipticities, and position angles, respectively. The SBPs are displayed in Figure 1 with the accompanying galaxy images. The error bar at each surface brightness level was computed from the quadrature sum of the uncertainty computed by the *ellipse* task and the uncertainty arising from the sky subtraction (see Section 4.2.2).

### 4.2. Profile Fitting

Most of the SBPs exhibit a central plateau and an exponential component extending down to a surface brightness of 23–24 mag arcsec$^{-2}$. This is consistent with the findings of Vaduvescu et al. (2005), who investigated the functions traditionally used to fit the SBPs of dIs and found that the near-infrared SBPs of many dIs closely follow a hyperbolic-secant (sech) function. In magnitude units, this fitting function is given by

$$\mu = \mu_0 - 2.5 \log \mathrm{sech}(r/r_0), \quad (1)$$

where $\mu$ is the surface brightness at radius $r$, $\mu_0$ is the central surface brightness, and $r_0$ is the scale length of the fit (i.e., the radius at which the intensity falls to 65% of the central value). At small radii, Equation (1) flattens out, converging to $\mu_0$. At large radii, Equation (1) approaches an exponential function with $r_0$ being the exponential scale length.

After calibrating the SBPs generated by the *ellipse* task using the measured zero points for each frame, we obtained the fit coefficients $\mu_0$ and $r_0$ for each galaxy using the STSDAS IRAF task *nfit1d* with the USERPAR/FUNCTION parameter set to Equation (1). The sech coefficients are given in Table 2. The sech fits are plotted on top of the SBPs in Figure 1. The average rms about the sech fit is 0.11 mag, with the largest rms of 0.23 mag associated with the IRSF observation of HIPASSJ1247−77.

Of the 80 dIs in this survey, we have identified 26 for which their SBPs exhibit a central peak, thereby deviating from the flattening of the sech function at small radii. This is likely due to starburst activity within the galaxy core (see Vaduvescu et al. 2006). In such cases, we attempted to obtain a better fit to the SBPs using either an exponential function or the sum of a sech and a Gaussian function. For all 26 galaxies, the sum of a sech and a Gaussian function resulted in a lower rms about the fit than with a sech or an exponential function alone. In Figure 1, the SBPs for these galaxies display both the sech and Gaussian fits.

#### 4.2.1. Radial Range of the Fits

The isophotes included in the fit to each SBP begin at the smallest semimajor axis for which an isophote could be identified by *ellipse*. This innermost isophote was usually within 5″ of the galaxy centroid. The outermost isophote to include in the fit was identified as the faintest isophote that can be recovered down to the background noise level of the image. In most of the SBPs, the semimajor axis corresponding to this limiting isophote was easily identifiable. However, in cases where the amplitude of the background residuals was particularly large, a definitive identification of the limiting isophote could not be made. A representative example is the SBP obtained with the ESO–SOFI for HIPASSJ1247–77, one of the faintest dIs in our survey. The sensitivity of the fitting parameters to the limiting semimajor axis can be evaluated by fitting the SBP out to a range of possible semimajor axes and investigating the change in the fitting parameters. When the SBP of HIPASSJ1247–77 is fit out to semimajor axes ranging from 50″ to 90″, neither $\mu_0$ nor $m_S$ varies by more than 0.1 mag, which is within the uncertainties in these quantities.

Several of the SBPs in Figure 1 exhibit bumps and dips, particularly at the galaxy core and at the outermost isophotes. The bumps and dips reflect background residuals and imperfect masking of resolved stars prior to generating the SBPs with the *ellipse* task. As can be seen in the SBP of HIPASSJ1247−77, the low surface brightness of this galaxy relative to the sky brightness makes its isophotes particular susceptible to imperfections

**Table 2**
Photometric Parameters

| Galaxy | $\alpha$ (J2000) (hh:mm:ss) | $\delta$ (J2000) (dd:′:″) | $e$ | $\phi$ (°) | $\mu_0$ (mag arcsec$^{-2}$) | $r_0$ (″) | $\mu_c$ (mag arcsec$^{-2}$) | $r_c$ (″) | $m_S$ (mag) | $m_T$ | Unc. flag (mag) | $r_I$ (″) | $m_I$ (mag) | Instrument |
|---|---|---|---|---|---|---|---|---|---|---|---|---|---|---|
| (1) | (2) | (3) | (4) | (5) | (6) | (7) | (8) | (9) | (10) | (11) | (12) | (13) | (14) | (15) |
| ANTLIA | 10:04:04 | −27:20:01. | 0.56 | −67 | 21.69 ± 0.20 | 35.2 ± 3.6 | ... | ... | 12.20 ± 0.37 | 12.73 ± 0.49 | * | 27.4 | 14.67 | SPM-CAMILA |
| CAMB | 04:53:07 | +67:05:55. | 0.56 | +55 | 21.95 ± 0.23 | 26.3 ± 1.1 | 21.81 | 3.3 | 13.09 ± 0.28 | 13.36 ± 0.31 | ... | 7.7 | 16.94 | CFHT-IR |
| CAS1 | 02:06:04 | +69:00:13. | 0.58 | +89 | 19.48 ± 0.09 | 52.8 ± 4.9 | ... | ... | 9.16 ± 0.24 | 9.34 ± 0.21 | ... | 156.0 | 9.52 | CFHT-WIRCAM |
| CGCG087-33 | 07:42:32 | +16:33:37. | 0.59 | +50 | 19.75 ± 0.08 | 13.8 ± 0.4 | ... | ... | 12.36 ± 0.17 | 12.53 ± 0.31 | ... | 36.5 | 12.83 | SPM-CAMILA |
| DDO120 | 12:21:13 | +45:52:43. | 0.50 | −77 | 20.59 ± 0.13 | 38.1 ± 1.7 | 21.05 | 12.6 | 10.79 ± 0.16 | 10.77 ± 0.31 | ... | 74.2 | 11.42 | CFHT-IR |
| DDO122 | 12:24:25 | +70:20:05. | 0.22 | +87 | 20.03 ± 0.15 | 26.4 ± 2.6 | 20.14 | 7.6 | 10.54 ± 0.21 | 10.55 ± 0.35 | ... | 64.2 | 10.93 | CFHT-IR |
| DDO125 | 12:27:42 | +43:29:41. | 0.41 | −68 | 20.24 ± 0.25 | 42.4 ± 0.6 | ... | ... | 10.02 ± 0.26 | 10.23 ± 0.27 | ... | 94.8 | 10.54 | CFHT-IR |
| DDO165 | 13:06:24 | +67:42:27. | 0.45 | −89 | 21.10 ± 0.09 | 42.3 ± 1.8 | ... | ... | 10.96 ± 0.20 | 11.14 ± 0.24 | ... | 59.8 | 12.01 | CFHT-IR |
| DDO168 | 13:14:27 | +45:55:26. | 0.62 | −33 | 20.36 ± 0.11 | 36.1 ± 1.0 | ... | ... | 10.97 ± 0.17 | 11.11 ± 0.26 | ... | 75.8 | 11.56 | CFHT-IR |
| DDO169 | 13:15:30 | +47:29:58. | 0.31 | +45 | 20.20 ± 0.13 | 16.1 ± 1.0 | ... | ... | 11.92 ± 0.22 | 12.17 ± 0.22 | ... | 37.5 | 12.56 | CFHT-IR |
| DDO181 | 13:39:52 | +40:48:26. | 0.30 | +78 | 20.77 ± 0.13 | 23.7 ± 0.7 | 22.47 | 3.6 | 11.64 ± 0.16 | 11.85 ± 0.18 | ... | 41.7 | 12.43 | CFHT-IR |
| DDO190 | 14:24:44 | +44:31:34. | 0.11 | −60 | 19.62 ± 0.26 | 19.5 ± 0.6 | ... | ... | 10.64 ± 0.30 | 10.72 ± 0.38 | ... | 55.6 | 10.93 | CFHT-IR |
| DDO210 | 20:46:52 | −12:50:54. | 0.18 | −68 | 20.90 ± 0.16 | 30.5 ± 0.8 | 22.14 | 4.1 | 11.05 ± 0.22 | 11.29 ± 0.27 | ... | 50.8 | 11.94 | CFHT-WIRCAM |
| DDO226 | 00:43:04 | −22:14:52. | 0.85 | 0 | 20.58 ± 0.11 | 42.8 ± 0.8 | ... | ... | 11.82 ± 0.13 | 12.48 ± 0.19 | ... | 84.0 | 12.81 | IRSF-SIRIUS |
| DDO43 | 07:28:18 | +40:46:07. | 0.49 | +20 | 20.65 ± 0.10 | 13.7 ± 0.2 | ... | ... | 13.04 ± 0.13 | 13.31 ± 0.15 | * | 26.1 | 13.70 | CFHT-IR |
| DDO46 | 07:41:26 | +40:06:55. | 0.34 | −70 | 21.70 ± 0.17 | 19.1 ± 0.9 | 21.55 | 4.1 | 13.10 ± 0.23 | 13.45 ± 0.26 | ... | 14.1 | 15.23 | CFHT-IR |
| DDO52 | 08:28:28 | +41:51:21. | 0.05 | 0 | 21.58 ± 0.12 | 22.7 ± 3.1 | 21.76 | 7.1 | 12.20 ± 0.27 | 12.37 ± 0.22 | ... | 20.9 | 13.77 | CFHT-IR |
| DDO53 | 08:34:08 | +66:10:47. | 0.14 | +90 | 22.16 ± 0.11 | 27.1 ± 0.5 | ... | ... | 12.51 ± 0.16 | 12.77 ± 0.18 | ... | ... | ... | CFHT-WIRCAM |
| DDO6 | 00:49:49 | −21:01:03. | 0.71 | +40 | 22.04 ± 0.10 | 36.7 ± 2.0 | ... | ... | 12.91 ± 0.26 | 13.26 ± 0.37 | * | ... | ... | IRSF-SIRIUS |
| DDO6 | 00:49:49 | −21:01:02. | 0.71 | +41 | 21.99 ± 0.03 | 26.2 ± 0.5 | ... | ... | 13.59 ± 0.11 | 14.01 ± 0.15 | * | 3.7 | 19.15 | NTT-SOFI |
| DDO87 | 10:49:37 | +65:31:48. | 0.50 | −87 | 21.51 ± 0.23 | 38.9 ± 1.9 | 22.04 | 11.9 | 11.66 ± 0.25 | 11.86 ± 0.32 | ... | 39.4 | 13.14 | CFHT-IR |
| DDO99 | 11:50:53 | +38:52:49. | 0.29 | +70 | 21.31 ± 0.42 | 30.7 ± 1.5 | 21.59 | 6.2 | 11.60 ± 0.45 | 11.86 ± 0.45 | ... | 37.5 | 12.93 | CFHT-IR |
| DW2 | 02:54:09 | +59:00:16. | 0.76 | +56 | 19.80 ± 0.12 | 63.2 ± 1.9 | ... | ... | 9.70 ± 0.16 | 10.22 ± 0.23 | ... | 163.8 | 10.52 | CFHT-WIRCAM |
| E215-09 | 10:57:30 | −48:10:48. | 0.17 | +5 | 20.98 ± 0.17 | 17.3 ± 0.8 | ... | ... | 12.34 ± 0.24 | 12.60 ± 0.38 | ... | 26.4 | 13.42 | IRSF-SIRIUS |
| E269-58 | 13:10:33 | −46:59:32. | 0.37 | +71 | 19.14 ± 0.22 | 36.2 ± 3.7 | 18.46 | 18.2 | 9.20 ± 0.10 | 9.04 ± 0.43 | ... | 115.6 | 9.19 | IRSF-SIRIUS |
| E321-14 | 12:13:49 | −38:13:46. | 0.73 | +33 | 21.21 ± 0.16 | 34.1 ± 1.4 | 21.55 | 6.0 | 12.31 ± 0.22 | 12.70 ± 0.25 | ... | 44.5 | 13.58 | IRSF-SIRIUS |
| E324-24 | 13:27:39 | −41:28:57. | 0.07 | +90 | 20.47 ± 0.17 | 36.0 ± 0.6 | ... | ... | 10.11 ± 0.20 | 10.35 ± 0.21 | ... | 72.6 | 10.79 | IRSF-SIRIUS |
| E325-11 | 13:45:01 | −41:51:33. | 0.63 | −46 | 21.01 ± 0.07 | 45.8 ± 1.8 | ... | ... | 11.13 ± 0.17 | 11.37 ± 0.21 | ... | 71.5 | 12.18 | CTIO-ISPI |
| E325-11 | 13:45:01 | −41:51:34. | 0.65 | −45 | 20.96 ± 0.13 | 48.1 ± 1.4 | ... | ... | 11.04 ± 0.18 | 11.32 ± 0.25 | ... | 76.2 | 12.04 | IRSF-SIRIUS |
| E349-31 | 00:08:14 | −34:34:40. | 0.42 | +18 | 21.51 ± 0.17 | 21.6 ± 0.8 | ... | ... | 12.77 ± 0.24 | 13.02 ± 0.32 | ... | 21.4 | 14.40 | IRSF-SIRIUS |
| E349-31 | 00:08:14 | −34:34:41. | 0.42 | +15 | 21.55 ± 0.05 | 18.8 ± 0.7 | ... | ... | 13.12 ± 0.23 | 13.37 ± 0.27 | * | 17.5 | 14.93 | NTT-SOFI |
| E379-07 | 11:54:43 | −33:33:36. | 0.15 | +90 | 22.12 ± 0.20 | 18.4 ± 1.4 | 21.16 | 1.9 | 13.32 ± 0.32 | 13.60 ± 0.48 | ... | ... | ... | IRSF-SIRIUS |

**Table 2**
(Continued)

| Galaxy | $\alpha$ (J2000) (hh:mm:ss) | $\delta$ (J2000) (dd:′:″) | $e$ | $\phi$ (°) | $\mu_0$ (mag arcsec$^{-2}$) | $r_0$ (″) | $\mu_c$ (mag arcsec$^{-2}$) | $r_c$ (″) | $m_S$ (mag) | $m_T$ | Unc. flag (mag) | $r_I$ (″) | $m_I$ (mag) | Instrument |
|---|---|---|---|---|---|---|---|---|---|---|---|---|---|---|
| (1) | (2) | (3) | (4) | (5) | (6) | (7) | (8) | (9) | (10) | (11) | (12) | (13) | (14) | (15) |
| E381-18 | 12:44:43 | −35:58:01. | 0.30 | +85 | 20.45 ± 0.10 | 9.1 ± 0.6 | ... | ... | 13.40 ± 0.21 | 13.52 ± 0.39 | ... | 18.8 | 13.97 | IRSF-SIRIUS |
| E381-20 | 12:46:01 | −33:50:17. | 0.68 | −49 | 21.01 ± 0.07 | 34.8 ± 0.6 | ... | ... | 11.89 ± 0.11 | 12.11 ± 0.14 | * | 53.3 | 12.83 | CTIO-ISPI |
| E384-16 | 13:57:01 | −35:19:58. | 0.08 | 0 | 19.47 ± 0.16 | 10.2 ± 0.3 | 20.40 | 4.5 | 11.86 ± 0.17 | 12.00 ± 0.18 | ... | 30.4 | 12.08 | IRSF-SIRIUS |
| E444-78 | 13:36:31 | −29:14:06. | 0.59 | +39 | 20.47 ± 0.05 | 19.3 ± 0.4 | ... | ... | 12.36 ± 0.11 | 12.64 ± 0.17 | ... | 39.1 | 13.07 | CFHT-IR |
| E444-84 | 13:37:20 | −28:02:37. | 0.11 | −1 | 20.62 ± 0.05 | 14.5 ± 0.3 | ... | ... | 12.28 ± 0.11 | 12.60 ± 0.13 | * | 28.0 | 12.98 | CFHT-IR |
| HIPASSJ1247-77 | 12:47:32 | −77:34:54. | 0.15 | +45 | 21.48 ± 0.12 | 8.6 ± 0.3 | ... | ... | 14.34 ± 0.27 | 14.39 ± 0.33 | * | 8.9 | 16.01 | IRSF-SIRIUS |
| HIPASSJ1247-77 | 12:47:32 | −77:34:54. | 0.18 | +43 | 21.55 ± 0.06 | 7.4 ± 0.4 | ... | ... | 14.76 ± 0.12 | 15.13 ± 0.23 | * | 6.9 | 16.78 | NTT-SOFI |
| HIPASSJ1337-39 | 13:37:25 | −39:53:52. | 0.83 | +37 | 21.65 ± 0.09 | 9.4 ± 0.7 | ... | ... | 16.07 ± 0.28 | 16.61 ± 0.52 | * | 7.6 | 18.39 | NTT-SOFI |
| HIPASSJ1348-37 | 13:48:32 | −37:57:42. | 0.47 | +69 | 20.55 ± 0.36 | 3.5 ± 0.4 | ... | ... | 15.88 ± 0.26 | 16.70 ± 0.62 | * | 7.0 | 17.72 | IRSF-SIRIUS |
| HIPASSJ1351-47 | 13:51:21 | −46:59:55. | 0.95 | +59 | 21.40 ± 0.14 | 29.5 ± 1.3 | 21.99 | 3.4 | 14.65 ± 0.16 | 15.79 ± 0.41 | * | 33.2 | 16.60 | IRSF-SIRIUS |
| HOI | 09:40:27 | +71:11:02. | 0.31 | −37 | 22.15 ± 0.09 | 63.2 ± 1.2 | ... | ... | 10.90 ± 0.14 | 11.20 ± 0.19 | * | ... | ... | CFHT-WIRCAM |
| I3104 | 12:18:46 | −79:43:40. | 0.55 | +36 | 19.00 ± 0.14 | 43.1 ± 0.9 | ... | ... | 9.04 ± 0.16 | 9.26 ± 0.20 | ... | 147.6 | 9.31 | IRSF-SIRIUS |
| I3687 | 12:42:15 | +38:30:15. | 0.40 | 0 | 20.72 ± 0.06 | 33.5 ± 1.4 | 21.23 | 12.8 | 11.00 ± 0.14 | 11.12 ± 0.23 | ... | 61.1 | 11.67 | CFHT-IR |
| I4182 | 13:05:49 | +37:36:16. | 0.21 | 0 | 20.42 ± 0.48 | 49.8 ± 1.1 | 21.29 | 17.4 | 9.54 ± 0.49 | 9.72 ± 0.50 | ... | 105.6 | 10.10 | CFHT-WIRCAM |
| I4247 | 13:26:44 | −30:21:47. | 0.65 | −28 | 18.82 ± 0.03 | 17.2 ± 0.3 | ... | ... | 11.13 ± 0.08 | 11.25 ± 0.22 | ... | 59.5 | 11.36 | SPM-CAMILA |
| I4316 | 13:40:18 | −28:53:33. | 0.60 | +63 | 20.10 ± 0.22 | 34.0 ± 1.2 | 20.13 | 13.9 | 10.78 ± 0.23 | 10.96 ± 0.32 | ... | 80.1 | 11.23 | SPM-CAMILA |
| I4662 | 17:47:08 | −64:38:32. | 0.27 | −69 | 17.42 ± 0.14 | 21.6 ± 0.4 | ... | ... | 8.44 ± 0.19 | 8.53 ± 0.31 | ... | 106.1 | 8.56 | IRSF-SIRIUS |
| I5152 | 22:02:42 | −51:17:46. | 0.34 | −74 | 18.09 ± 0.18 | 38.0 ± 1.6 | 18.11 | 14.4 | 8.00 ± 0.18 | 7.97 ± 0.29 | ... | 155.6 | 8.03 | IRSF-SIRIUS |
| KDG52 | 08:23:56 | +71:01:50. | 0.42 | −7 | 22.81 ± 0.16 | 34.0 ± 2.6 | ... | ... | 13.08 ± 0.28 | 13.63 ± 0.19 | * | ... | ... | CFHT-WIRCAM |
| KK17 | 02:00:10 | +28:49:51. | 0.69 | −31 | 21.69 ± 0.09 | 19.7 ± 0.5 | 22.63 | 3.0 | 13.84 ± 0.12 | 14.24 ± 0.26 | ... | 15.0 | 16.25 | CFHT-WIRCAM |
| KK182 | 13:05:02 | −40:04:58. | 0.32 | +78 | 21.31 ± 0.03 | 14.5 ± 0.4 | ... | ... | 13.27 ± 0.23 | 13.47 ± 0.29 | ... | 17.6 | 14.50 | IRSF-SIRIUS |
| KK182 | 13:05:02 | −40:04:58. | 0.32 | +72 | 21.35 ± 0.12 | 10.5 ± 0.4 | ... | ... | 14.02 ± 0.22 | 14.23 ± 0.34 | * | 12.4 | 15.38 | NTT-SOFI |
| KK195 | 13:21:08 | −31:31:51. | 0.48 | +4 | 22.02 ± 0.11 | 7.0 ± 0.5 | ... | ... | 15.87 ± 0.22 | 16.26 ± 0.50 | * | ... | ... | IRSF-SIRIUS |
| KK230 | 14:07:11 | +35:03:35. | 0.05 | 0 | 22.57 ± 0.18 | 14.7 ± 0.5 | 22.80 | 2.7 | 14.14 ± 0.23 | 14.55 ± 0.29 | * | ... | ... | CFHT-WIRCAM |
| KKH11 | 02:24:35 | +56:00:38. | 0.45 | −40 | 19.95 ± 0.14 | 19.3 ± 0.2 | ... | ... | 11.51 ± 0.16 | 11.74 ± 0.17 | ... | 47.9 | 12.03 | CFHT-IR |
| KKH12 | 02:27:28 | +57:29:18. | 0.55 | −15 | 20.17 ± 0.14 | 23.5 ± 0.7 | ... | ... | 11.53 ± 0.17 | 11.79 ± 0.24 | ... | 53.3 | 12.29 | CFHT-WIRCAM |
| KKH6 | 01:34:52 | +52:05:35. | 0.10 | +15 | 20.66 ± 0.17 | 9.0 ± 0.1 | ... | ... | 13.35 ± 0.20 | 13.73 ± 0.21 | * | 17.1 | 14.12 | CFHT-WIRCAM |
| KKH60 | 10:16:00 | +06:48:17 | 0.68 | +72 | 22.36 ± 0.23 | 23.5 ± 2.6 | 22.00 | 4.5 | 14.09 ± 0.38 | 14.55 ± 0.38 | ... | ... | ... | IRSF-SIRIUS |
| KKH86 | 13:54:33 | +04:14:45 | 0.39 | −3 | 21.57 ± 0.08 | 14.3 ± 0.5 | ... | ... | 13.68 ± 0.13 | 14.09 ± 0.17 | * | 12.9 | 15.62 | IRSF-SIRIUS |
| KKH98 | 23:45:34 | +38:42:55. | 0.41 | −5 | 21.44 ± 0.15 | 16.0 ± 0.3 | ... | ... | 13.35 ± 0.20 | 13.82 ± 0.24 | * | 17.0 | 15.40 | CFHT-WIRCAM |
| N4523 | 12:33:48 | +15:10:06. | 0.20 | +35 | 19.89 ± 0.05 | 23.8 ± 0.9 | 19.84 | 6.8 | 10.60 ± 0.11 | 10.73 ± 0.15 | ... | 59.9 | 10.97 | CFHT-IR |

**Table 2**
(Continued)

| Galaxy | $\alpha$ (J2000) (hh:mm:ss) | $\delta$ (J2000) (dd:′:″) | $e$ | $\phi$ (°) | $\mu_0$ (mag arcsec$^{-2}$) | $r_0$ (″) | $\mu_c$ (mag arcsec$^{-2}$) | $r_c$ (″) | $m_S$ (mag) | $m_T$ | Unc. flag (mag) | $r_I$ (″) | $m_I$ (mag) | Instrument |
|---|---|---|---|---|---|---|---|---|---|---|---|---|---|---|
| (1) | (2) | (3) | (4) | (5) | (6) | (7) | (8) | (9) | (10) | (11) | (12) | (13) | (14) | (15) |
| P45628 | 13:09:37 | −27:08:28. | 0.51 | −36 | 19.56 ± 0.23 | 24.9 ± 0.6 | ... | ... | 10.70 ± 0.27 | 10.80 ± 0.43 | ... | 72.7 | 11.10 | SPM-CAMILA |
| P47885[a] | 13:35:08 | −30:07:02. | 0.72 | −60 | 17.41 ± 0.12 | 8.3 ± 0.3 | 16.00 | 2.8 | 11.55 ± 0.14 | 11.66 ± 0.42 | ... | 40.4 | 11.68 | NTT-SOFI |
| PEGDIG | 23:28:37 | +14:44:32. | 0.45 | −65 | 20.96 ± 0.09 | 78.8 ± 0.6 | ... | ... | 9.48 ± 0.12 | 9.87 ± 0.12 | * | 122.2 | 10.44 | CFHT-WIRCAM |
| SAGDIG | 19:29:59 | −17:40:51. | 0.16 | +90 | 21.95 ± 0.38 | 36.9 ± 1.3 | ... | ... | 11.65 ± 0.44 | 12.13 ± 0.45 | * | 11.2 | 15.68 | CFHT-WIRCAM |
| SEXA | 10:11:03 | −04:41:01 | 0.05 | 0 | 20.90 ± 0.09 | 30.1 ± 0.5 | ... | ... | 10.91 ± 0.14 | 11.25 ± 0.16 | * | 48.4 | 12.00 | CTIO-ISPI |
| SEXA | 10:11:03 | −04:41:01 | 0.05 | 0 | 21.10 ± 0.14 | 52.3 ± 4.2 | ... | ... | 9.91 ± 0.30 | 10.18 ± 0.25 | ... | 76.2 | 11.18 | IRSF-SIRIUS |
| SEXB | 10:00:00 | +05:19:47 | 0.13 | +90 | 20.58 ± 0.17 | 37.0 ± 2.2 | ... | ... | 10.23 ± 0.29 | 10.38 ± 0.37 | ... | 72.6 | 10.85 | IRSF-SIRIUS |
| U2684 | 03:20:23 | +17:17:47. | 0.72 | −79 | 21.18 ± 0.15 | 20.6 ± 0.6 | 21.87 | 1.6 | 13.34 ± 0.19 | 13.46 ± 0.25 | ... | 28.0 | 14.48 | CFHT-IR |
| U3755 | 07:13:52 | +10:31:16. | 0.50 | −80 | 19.84 ± 0.14 | 22.4 ± 0.5 | ... | ... | 11.19 ± 0.17 | 11.66 ± 0.37 | ... | 59.0 | 11.91 | SPM-CAMILA |
| U3817 | 07:22:44 | +45:06:29. | 0.08 | 0 | 21.00 ± 0.07 | 23.1 ± 0.4 | ... | ... | 11.62 ± 0.16 | 11.89 ± 0.17 | * | 35.7 | 12.76 | CFHT-IR |
| U4483 | 08:37:04 | +69:46:28. | 0.45 | −4 | 20.71 ± 0.17 | 17.9 ± 0.4 | ... | ... | 12.44 ± 0.21 | 12.70 ± 0.24 | * | 32.4 | 13.16 | CFHT-IR |
| U5288 | 09:51:17 | +07:49:40 | 0.82 | −23 | 19.81 ± 0.30 | 37.9 ± 3.5 | 18.78 | 15.3 | 11.13 ± 0.30 | 11.49 ± 0.31 | ... | 99.3 | 11.67 | CFHT-WIRCAM |
| U5423 | 10:05:31 | +70:21:53. | 0.51 | −38 | 19.61 ± 0.19 | 14.8 ± 0.8 | ... | ... | 11.88 ± 0.24 | 11.99 ± 0.39 | ... | 41.8 | 12.19 | CFHT-IR |
| U5829 | 10:42:44 | +34:27:04. | 0.36 | +80 | 20.65 ± 0.18 | 32.6 ± 2.0 | ... | ... | 10.91 ± 0.25 | 11.17 ± 0.24 | ... | 60.1 | 11.72 | CFHT-IR |
| U7298 | 12:16:19 | +52:13:01. | 0.59 | −39 | 21.96 ± 0.18 | 29.4 ± 4.4 | 21.93 | 5.4 | 12.93 ± 0.43 | 13.29 ± 0.65 | * | 8.1 | 16.65 | SPM-CAMILA |
| U7559 | 12:27:05 | +37:08:30. | 0.48 | −46 | 20.87 ± 0.13 | 34.5 ± 0.8 | ... | ... | 11.24 ± 0.22 | 11.53 ± 0.23 | ... | 58.2 | 12.32 | CFHT-IR |
| U7605 | 12:28:38 | +35:43:07. | 0.33 | −25 | 20.75 ± 0.19 | 19.2 ± 0.5 | ... | ... | 12.11 ± 0.23 | 12.40 ± 0.31 | ... | 34.4 | 13.06 | CFHT-WIRCAM |
| U8638 | 13:39:19 | +24:46:37. | 0.43 | +75 | 21.24 ± 0.20 | 38.4 ± 0.6 | ... | ... | 11.27 ± 0.23 | 11.53 ± 0.37 | ... | 49.2 | 12.47 | SPM-CAMILA |
| U8833 | 13:54:49 | +35:50:18. | 0.23 | −17 | 20.94 ± 0.15 | 18.7 ± 1.1 | ... | ... | 12.20 ± 0.24 | 12.31 ± 0.65 | ... | 30.1 | 13.19 | SPM-CAMILA |
| UA292 | 12:38:41 | +32:45:50. | 0.06 | 0 | 23.03 ± 0.10 | 20.9 ± 0.7 | ... | ... | 13.85 ± 0.21 | 14.24 ± 0.30 | * | ... | ... | CFHT-WIRCAM |
| UA319 | 13:02:14 | −17:14:16. | 0.72 | +30 | 20.20 ± 0.18 | 28.5 ± 1.9 | ... | ... | 11.66 ± 0.24 | 12.07 ± 0.35 | ... | 65.7 | 12.30 | CFHT-IR |
| UA438 | 23:26:27 | −32:23:19. | 0.10 | −60 | 20.48 ± 0.40 | 27.0 ± 0.7 | ... | ... | 10.78 ± 0.43 | 11.04 ± 0.45 | ... | 54.1 | 11.66 | IRSF-SIRIUS |
| UA438 | 23:26:27 | −32:23:20. | 0.10 | −60 | 20.58 ± 0.10 | 23.9 ± 2.7 | ... | ... | 11.16 ± 0.29 | 11.35 ± 0.26 | ... | 46.4 | 11.92 | NTT-SOFI |
| UA86 | 03:59:47 | +67:08:08. | 0.39 | +25 | 19.44 ± 0.14 | 74.1 ± 3.7 | ... | ... | 7.98 ± 0.19 | 8.17 ± 0.18 | ... | 219.5 | 8.34 | CFHT-WIRCAM |

**Notes.** (1) Name of galaxy. (2–5) Centroid, ellipticity ($1 - b/a$) and position angle (eastward from north) of the elliptical fit. For a discussion of the uncertainties in these quantities, see Section 4.1. (6 and 7) Central surface brightness and scale length of the sech fit to the SBP in $K_s$. For a discussion of the uncertainties in these quantities, see Section 4.2.2. (8 and 9) Central surface brightness and scale length of the Gaussian component of the profile fit (see Section 4.2). (10) Sech magnitude in $K_s$. The uncertainty is the quadrature sum of the scatter about the sech fit, the uncertainty in the frame zero point, and the uncertainty due to sky subtraction (see Section 4.2.2). (11) Total magnitude in $K_s$. The uncertainty is the quadrature sum of the measurement uncertainty in the total flux, the uncertainty in the frame zero point, the uncertainty due to sky subtraction, and the uncertainty in the asymptotic component of the total magnitude. (12) Uncertainty flag on the sech fit (see Section 4.4.1). (13) The semimajor axis of the $K_s$-isophote at 22 mag arcsec$^{-2}$. (14) Magnitude in $K_s$ within $r_{22}$. (15) Telescope and detector with which the image was acquired.

[a] The profile of P47885 suggests the presence of a central bulge, and spiral structure can be seen in its $K_s$ image.

in the mask. To evaluate the extent to which this affects its fitting parameters, we compare the fit to its SBP to the fit after deleting the isophotes in the dips at $\sim$15″, $\sim$40″, and $\sim$60″. The exclusion of the dips induced decreases of only 0.13 mag, 0.″8, and 0.04 mag in $\mu_0$, $r_0$, and $m_S$, respectively. As HIPASSJ1247−77 is representative of the lowest surface brightness objects in our survey, such bumps and dips in the SBPs do not appear to be a significant source of uncertainty in the photometric parameters.

#### 4.2.2. Uncertainties in the Fit Parameters

The formal uncertainties in $\mu_0$ and $r_0$, as computed by *nfit1d*, were typically found to be 0.02 mag arcsec$^{-2}$ and 0.″3, respectively. An additional and important source of uncertainty in these parameters arises from the sky subtraction process. If the sky image does not accurately match the underlying background pattern on the galaxy image, the galaxy image will be contaminated by positive or negative background residuals. If there is an excess of the latter, the profile will appear steeper at high radii, resulting in a truncated value for $r_0$. In the former case, the profile will appear flatter, resulting in a larger $r_0$ and correspondingly brighter integrated magnitude.

We have accounted for this source of uncertainty using a method similar to that discussed in Cairós et al. (2003). Specifically, for each galaxy image, we added a constant offset $\pm\Delta$sky, which represents the upper and lower limits of the background residuals. $\Delta$sky was computed from the median absolute deviation of the background estimated from a star- and galaxy-free region of each image. The resulting upper and lower galaxy images were used to regenerate the SBP and determine the upper and lower limits for each fit parameter. The differences between the upper and lower limits and the mean values were generally symmetric, allowing us to adopt half the difference between the upper and lower limits of each fit parameter as its uncertainty due to sky subtraction. The uncertainties in $\mu_0$ and $r_0$ that are listed in Table 2 are therefore the quadrature sum of the formal uncertainty computed by *nfit1d* and the uncertainty in the sky subtraction. The uncertainty in $\mu_0$ also includes the uncertainty in the photometric zero point measured for the galaxy frame.

### 4.3. Astrometry

Table 2 lists the right ascension and declination of the center of each galaxy's light profile found with the *ellipse* task. The coordinates are in the J2000.0 International Celestial Reference System. The plate solution for each galaxy image was computed using the stars on the image that were matched with 2MASS stars during the calibration process (see Section 3.3). For the six galaxy fields with fewer than three 2MASS stars, other stars in these fields were matched with stars in the U.S. Naval Observatory all-sky catalog version B1.0 (USNO-B1). The plate solutions were then used to transform the centroid of each light profile from pixel to celestial coordinates.

The accuracy in the astrometry is limited by the uncertainties in the catalogcoordinates and the accuracy of the ellipse centering algorithm and plate solution. According to the 2MASS PSC documentation,[13] 2MASS star coordinates are accurate to <0.″1 over most of their magnitude range. Typical uncertainties in the adopted galaxy centroids, as reported by *ellipse*, are 0.″7 (see Section 4.1). The average uncertainty in the plate solutions, as reported by IRAF's *ccmap* task, is 0.″2. Thus, the formal uncertainty in the galaxy coordinates listed in Table 2 is $\sim$1″.

[13] http://www.ipac.caltech.edu/2mass/releases/allsky/doc/sec6_1d.html

### 4.4. Integrated Magnitudes

We computed two types of magnitudes to quantify the total amount of light emitted in $K_s$. One is the sech magnitude, $m_S$, which is computed from the integral of a dI's sech fit out to infinity, i.e.,

$$m_S = \mu_0 - 2.5 \log 11.511 r_0^2 (1 - e), \quad (2)$$

where $e$ is the ellipticity obtained with the *ellipse* task (see Section 4.1). In principle, $m_S$ is the best measure of the brightness of the old population of a dI because it is least affected by deviations arising from recent star formation. The uncertainty in $m_S$ is the quadrature sum of the scatter about the sech fit, the uncertainty in the zero point measured for the galaxy frame, and the uncertainty due to sky subtraction (see Section 4.2.2). Our measurements of $m_S$ and its associated uncertainty are given in Table 2. The average uncertainty in $m_S$ is 0.23 mag.

We have also measured the total magnitude, $m_T$, which is computed from the integral of the flux at each elliptical isophote generated by the *ellipse* task, added to the integral of an exponential from the maximum semimajor axis reached by *ellipse* out to infinity. Given that resolved stars are masked so that their light does not contribute to the isophotal intensities computed by *ellipse*, $m_T$ and $m_S$ should closely agree, except in those cases where starburst activity in a galaxy's core or elsewhere causes its light profile to deviate from the sech function. For the 54 profiles which have been fit to a sech function alone, the average difference in $m_S$ and $m_T$ is only $0.28 \pm 0.17$ mag (i.e., comparable to the average measurement uncertainty in $m_S$). The sech fits can therefore be considered a reliable gauge of the light profiles of the dIs in this survey.

For each SBP, we have also measured the isophotal magnitude, $m_{22}$, which is the total flux, in magnitudes, within the isophote at 22 mag arcsec$^{-2}$. In combination with $m_T$, $m_{22}$ provides a fit-independent gauge of a dI's light distribution. This quantity is listed in Table 2, along with the radius corresponding to this isophote ($r_{22}$).

Extinctions, distances, and absolute $K_s$ magnitudes for the dIs in this survey will be presented in Paper II.

#### 4.4.1. Comparison with Different Facilities

As described in Section 3, all of the galaxies in this survey have been observed in a similar manner and images have been processed in a similar fashion to ensure that our data set is self-consistent. To confirm this, we compare a few dIs observed with multiple facilities. These objects are E325–11, SEXA, UA438, KK182, E349–31, DDO6, and HIPASSJ1247–77. The latter four of these targets are among the lowest surface-brightness objects in our survey, having central surface brightnesses fainter than 21.5 mag arcsec$^{-2}$. In Figure 2, we overplot the SBPs obtained from each site. For each dI, the isophotes obtained from the different sites differ by a mean value of only $0.15 \pm 0.03$ mag within 0.5 mag arcsec$^{-2}$ of the central surface brightness of the deeper profile (i.e., within 1 sech scale length). This difference is comparable to the uncertainty in the central surface brightness, which confirms the reliability of the frame zero points and the integrity of the subtraction of the sky background level. The mean difference between isophotes from different sites increases slightly to $0.18 \pm 0.05$ mag within 1.4 mag arcsec$^{-2}$ of the central surface brightness (i.e., within 2 sech scale lengths). Within 2.5 mag arcsec$^{-2}$ of the central surface brightness (3 sech scale lengths), the mean difference between isophotes increases to $0.20 \pm 0.05$ mag, which is within the uncertainty associated

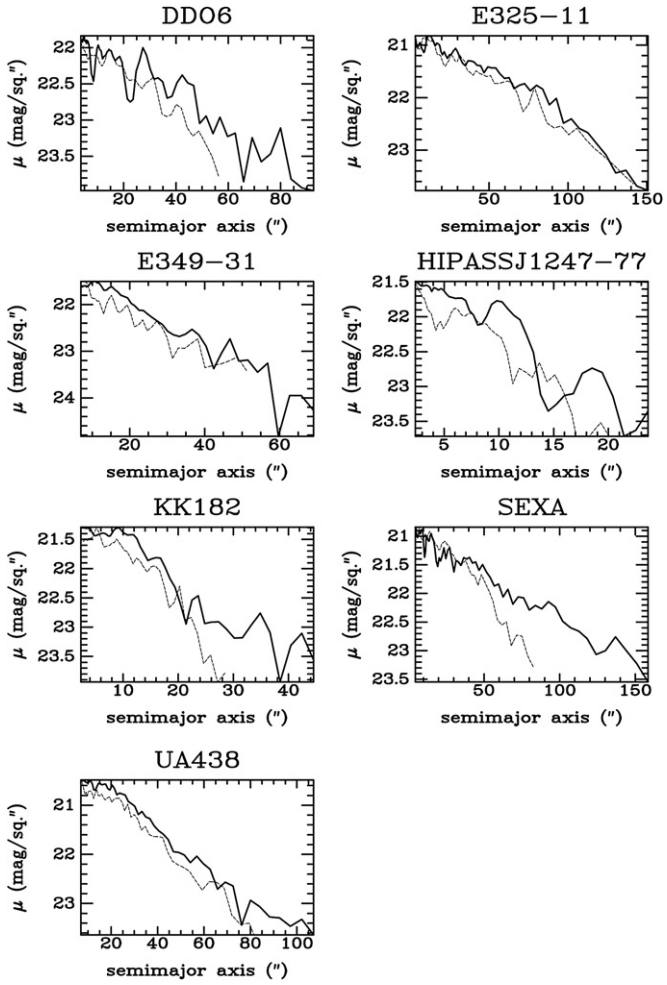


**Figure 2.** Solid line is the SBP obtained with the IRSF. The dashed line is the SBP obtained with the comparison facility (ESO–SOFI or CTIO–ISPI).

with the estimation of the sky background for these galaxies (see Section 4.2.2), this uncertainty being the primary cause of discrepancies in the outer isophotes of the SBPs obtained from different sites.

In the case of all seven galaxies, the deepest profiles were obtained with the IRSF, where the amplitude of the sky residuals was lowest. The lower this amplitude, the fainter the outermost isophote that can be distinguished from the background residuals. With the exception of the two faint dIs DDO6 and HIPASSJ1247–77, the IRSF profiles for these galaxies have depths of at least 2.5 mag arcsec$^{-2}$ in surface brightness. In comparison, the CTIO–ISPI and ESO–SOFI profiles for the same galaxies only exceed three sech scale lengths for E325–11 and UA438. In all seven cases, the non-photometric conditions during the CTIO-ISPI and ESO-SOFI runs led to smaller scale lengths than measured from the IRSF profiles for the same galaxies. This can be seen most dramatically in the SBPs for DDO6, KK182, and SEXA, where the high background residuals in the CTIO–ISPI and ESO–SOFI images have resulted in an oversubtraction of the sky. For E325-11, E349–31, and UA438, the corresponding dimming effect on $m_S$ is small, as the measurements of $m_S$ from different sites are consistent within the uncertainty in this quantity. However, for the other four galaxies, the discrepancy in the measurements of $m_S$ from different sites is within 0.5–1.0 mag. This demonstrates the importance of isophotes well beyond the flat core in properly defining the slope of a dI's SBP. Based on this comparison, we caution that integrated magnitudes should be treated as faint limits in cases where the faintest detectable isophote is within 2.5 mag arcsec$^{-2}$ of the central surface brightness. The 28 profiles that do not meet this sensitivity criterion are indicated in Table 2. For the seven dIs for which images were obtained at multiple sites, we have adopted the photometric parameters measured from the IRSF images for all further analyses.

#### 4.4.2. Comparison with 2MASS Photometric Parameters

Four dIs in our survey (I3104, I4662, I5152, and P47885) have $K_s$ photometry published in the 2MASS Extended Source Catalogue. In Table 3, we show how the 2MASS photometric parameters compare with the same quantities measured from our survey.

The 2MASS quantity *k_m_5* is the integrated magnitude within a circular aperture of 5″ in radius. We have measured this quantity from our images of the four 2MASS galaxies and find values that are reasonably consistent with 2MASS. Again, this confirms the reliability of our sky subtraction and photometric zero points. The largest difference of 0.4 mag observed with I3104 is most likely due to the galaxy centroid adopted by 2MASS, which differs from ours by over 30″. Also, the 2MASS light profile for this galaxy is defined out to only 14″, which is less than 10% of the galaxy's detectable extent in our deeper IRSF image and less than half of its sech scale length. With such a limited sampling, it is unlikely that the 2MASS centroid accurately coincides with the center of the galaxy.

The 2MASS extrapolated magnitude *k_m_ext* is the isophotal magnitude at the 20 mag arcsec$^{-2}$ isophote added to the integral of the fit from this isophote out to the radius *r_ext*, which is the deduced extent of the 2MASS profile. For each of the dIs in Table 3, we have used our *ellipse* output to compute the integrated magnitude out to the 2MASS value of *r_ext*. Our values of *k_m_ext* are significantly brighter than the 2MASS values, despite the close match in *k_m_5*. This indicates that the slopes of the profile fits obtained by 2MASS are steeper than the true profiles, which explains the significant discrepancy between the values of *k_m_ext* reported by 2MASS and our measurements of $m_T$. Table 3 is sorted in the order of descending *%r_ext*, the ratio in percent of the 2MASS measurement of *r_ext* to the measurement obtained from our deeper profiles. This emphasizes that the discrepancy between *k_m_ext* and $m_T$ can be significant when the 2MASS integration aperture is not representative of the full galaxy extent. As was found in the previous section, this demonstrates the importance of detecting isophotes well beyond a dI's core in order to arrive at a reliable total magnitude.

#### 4.4.3. The dI Fundamental Plane

Vaduvescu & McCall (2008) have constructed the Fundamental Plane for dIs using $K_s$ photometry and TRGB distances for a sample of 34 dIs in the Local Volume. This relationship is a correlation between a dI's central surface brightness, the motions of its gas, and its total stellar mass; the latter of which has been quantified by these authors using the sech magnitude $m_S$. The rms of the correlation for the 34 dIs is 0.43 mag. For the 28 dIs in this paper with both TRGB distances and published H I line widths, the scatter about the Fundamental Plane is 0.46 mag (comparable to the findings of Vaduvescu & McCall 2008), which demonstrates the self-consistency of our data. In addition, O. Vaduvescu et al. (2010, in preparation) have combined the $K_s$ photometry in this survey for these 28 dIs with

**Table 3**
Comparison with 2MASS Photometric Parameters

| Galaxy | *k_m_5* | | *r_ext* | | *k_m_ext* | | | | |
|---|---|---|---|---|---|---|---|---|---|
| | 2MASS (mag) | This Paper (mag) | 2MASS (″) | This Paper (″) | 2MASS (mag) | This Paper (mag) | $m_T$ (mag) | %*r_ext* (%) | $\Delta m$ (mag) |
| (1) | (2) | (3) | (4) | (5) | (6) | (7) | (8) | (9) | (10) |
| I3104 | 14.25 | 14.57 | 14 | 148 | 13.61 | 9.31 | 9.26 | 9 | 4.35 |
| I5152 | 12.80 | 12.52 | 67 | 199 | 9.28 | 7.98 | 7.97 | 34 | 1.31 |
| P47885 | 12.47 | 12.40 | 22 | 52 | 11.74 | 11.66 | 11.66 | 43 | 0.08 |
| I4662 | 12.82 | 12.76 | 68 | 123 | 9.51 | 8.54 | 8.53 | 55 | 0.98 |

**Notes.** (1) Name of galaxy. (2) Integrated $K_s$ magnitude within a 5″ circular aperture as measured from the 2MASS image. (3) $K_s$ integrated magnitude within a 5″ circular aperture as measured from our image. (4) Extent of the galaxy's light profile in $K_s$ as deduced from the 2MASS surface photometry. (5) Extent of the galaxy's light profile in $K_s$ as deduced from our surface photometry. (6) Integrated $K_s$ magnitude from the 2MASS fit to the SBP out to *r_ext*. (7) Integrated $K_s$ magnitude from our SBP out to the 2MASS measurement of *r_ext*. (8) Total magnitude in $K_s$ as deduced from our surface photometry. (9) Ratio in percent of the 2MASS measurement of *r_ext* to our measurement. (10) Difference between the 2MASS measurement of *k_m_ext* and our measurement of $m_T$.

∼50 other dIs in the Local Volume to expand the luminosity range of the dI Fundamental Plane. The rms of the Fundamental Plane correlation for their sample of nearly 80 dIs is ∼0.4 mag. This is comparable to the scatter of ∼0.35 mag characteristic of the Tully–Fisher relation for spirals (see, for example, Sakai et al. 2000). Thus, the sech magnitudes derived in this survey can be considered reliable estimates of the total stellar masses of the dIs.

## 5. SUMMARY

We have obtained deep $K_s$ images for 86 dIs situated within ∼5 Mpc of the Milky Way. Of these, 80 were detected sufficiently well for us to identify elliptical isophotes and therefore conduct surface photometry. For each of these galaxies, we present its SBP, the ellipse parameters used to generate the profile, the parameters of the sech fit to the profile, the total magnitude computed from the data as well as from the fit, and an isophotal magnitude and radius. Extinctions, distances, and absolute $K_s$ magnitudes for the dIs in this survey will be presented in Paper II, where the photometry will be used to investigate how the properties of local dIs depend upon environment.

Of the 80 dIs for which profile fits have been obtained, 54 have SBPs which closely match a sech fit (i.e., with an rms about the fit within 0.2 mag). The remaining 26 dIs have SBPs which are better represented by a sech plus a Gaussian, indicative of recent starburst activity in the core.

For the dIs fitted with a sech function alone, the total magnitude $m_T$ and the sech magnitude $m_S$ have an average difference of only $0.28 \pm 0.17$ mag. This confirms the findings of Vaduvescu et al. (2005) that the sech function reliably traces the light from the dI stellar population which dominates the total light from the galaxy in $K_s$.

The self-consistency of our photometric parameters is demonstrated in three ways. First, the central surface brightnesses measured for the galaxies that were observed at more than one facility are consistent within errors. This implies that external errors due to the photometric calibration and sky subtraction are small. Secondly, we have found the same consistency in the central surface brightnesses measured for the dIs with $K_s$ photometry published in the 2MASS Extended Source Catalogue. However, we find that the total $K_s$ magnitude measured for a dI can be significantly underestimated if isophotes beyond ∼3 scale lengths are not detected. Based on these analyses, we have identified 28 SBPs in our survey for which $m_S$ and $m_T$ should be treated as faint limits (and the sech scale lengths should be treated as lower limits). Lastly, the self-consistency of our data is revealed by the close fit to the dI Fundamental Plane derived by Vaduvescu & McCall (2008). Specifically, for the 28 dIs in this paper with both TRGB distances and published H I line widths, the scatter about the Fundamental Plane is 0.46 mag. This is comparable to the scatter of 0.43 mag found by Vaduvescu & McCall (2008) using a different sample of dIs. The scatter is also comparable to the Tully–Fisher relation for spirals, which supports the existence of a Fundamental Plane for dIs.

R.L.F. and M.L.M. gratefully acknowledge the continuing support of the Natural Sciences and Engineering Research Council of Canada. The authors would also like to thank the referee for extremely constructive comments, which have helped to strengthen the methods behind the results of this paper.

## REFERENCES

Cairós, L. M., et al. 2003, ApJ, 593, 312
Cruz-González, I., et al. 1994, Proc. SPIE, 2198, 774
Hunter, D. A., & Elmegreen, B. G. 2006, ApJS, 162, 49
Karachentsev, I. D., Karachentseva, V. E., Huchtmeier, W. K., & Makarov, D. I. 2004, AJ, 127, 2031
Karachentsev, et al. 2002, A&A, 389, 812
Kirby, E. M., Jerjen, H., Ryder, S. D., & Driver, S. P. 2008, AJ, 136, 1866
Noeske, K. G., Papaderos, P., Cairós, L. M., & Fricke, K. J. 2003, A&A, 410, 481
Peebles, P. J. E., Phelps, S. D., Shaya, E. J., & Tully, R. B. 2001, ApJ, 554, 104
Sakai, et al. 2000, ApJ, 529, 698
Schmidt, K.-H., & Boller, T. 1992, Astron. Nachr., 313, 329
Vaduvescu, O., & McCall, M. L. 2004, PASP, 116, 640
Vaduvescu, O., & McCall, M. L. 2008, A&A, 487, 147
Vaduvescu, O., McCall, M. L., & Richer, M. G. 2007, AJ, 134, 604
Vaduvescu, O., McCall, M. L., Richer, M. G., & Fingerhut, R. L. 2005, AJ, 130, 1593
Vaduvescu, O., Richer, M. G., & McCall, M. L. 2006, AJ, 131, 1318